ACS APPLIED MATERIALS & INTERFACES

www.acsami.org

Research Article

Polyphenolic Carbon Quantum Dots with Intrinsic Reactive Oxygen Species Amplification for Two-Photon Bioimaging and In Vivo Tumor Therapy

Sayan Deb Dutta,[▽] Md Moniruzzaman,[▽] Jin Hexiu,[▽] Sourav Sarkar, Keya Ganguly, Dinesh K. Patel, Jagannath Mondal, Yong-Kyu Lee, Rumi Acharya, Jongsung Kim,* and Ki-Taek Lim*

Cite This: *ACS Appl. Mater. Interfaces* 2023, 15, 52083−52099

Read Online

ACCESS | Metrics & More | Article Recommendations | Supporting Information

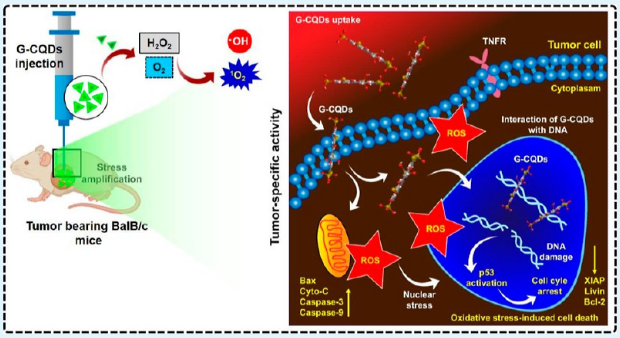

ABSTRACT: Recent studies indicate that mitochondrial dysfunctions and DNA damage have a critical influence on cell survival, which is considered one of the therapeutic targets for cancer therapy. In this study, we demonstrated a comparative study of the effect of polyphenolic carbon quantum dots (CQDs) on in vitro and in vivo antitumor efficacy. Dual emissive (green and yellow) shape specific polyphenolic CQDs (G-CQDs and Y-CQDs) were synthesized from easily available nontoxic precursors (phloroglucinol), and the antitumor property of the as-synthesized probe was investigated as compared to round-shaped blue emissive CQDs (B-CQDs) derived from well-reported precursor citric acid and urea. The B-CQDs had a nuclei-targeting property, and G-CQDs and Y-CQDs had mitochondria-targeting properties. We have found that the polyphenol containing CQDs (at a dose of 100 μg mL^{-1}) specifically attack mitochondria by excess accumulation, altering the metabolism, inhibiting branching pattern, imbalanced *Bax*/*Bcl-2* homeostasis, and ultimately generating oxidative stress levels, leading to oxidative stress-induced cell death in cancer cells in vitro. We show that G-CQDs are the main cause of oxidative stress in cancer cells because of their ability to produce sufficient $^\bullet$OH$^-$ and ^{1}O$_2$ radicals, evidenced by electron paramagnetic resonance spectroscopy and a terephthalic acid test. Moreover, the near-infrared absorption properties of the CQDs were exhibited in two-photon (TP) emission, which was utilized for TP cellular imaging of cancer cells without photobleaching. The in vivo antitumor test further discloses that intratumoral injection of G-CQDs can significantly augment the treatment efficacy of subcutaneous tumors without any adverse effects on BalB/c nude mice. We believe that shape-specific polyphenolic CQD-based nanotheranostic agents have a potential role in tumor therapy, thus proving an insight on treatment of malignant cancers.

KEYWORDS: *polyphenolic CQDs, mitochondrial dysfunctions, two-photon imaging, oxidative stress, nanotheranostics*

Downloaded via KANGWON NATL UNIV on November 16, 2023 at 06:33:18 (UTC).
See https://pubs.acs.org/sharingguidelines for options on how to legitimately share published articles.

1. INTRODUCTION

Mitochondria play a significant role in development,[1] cellular homeostasis,[2,3] signaling[2,4] and apoptosis by maintaining a balance between reactive oxygen species (ROS) and reducing species, such as hydrogen peroxide (H$_2$O$_2$) and glutathione (GSH).[2] Mitochondria-targeted cancer therapy includes the development of novel materials that could sufficiently alter the mitochondrial GSH, antioxidants, and amplify the ROS level to induce apoptotic cell death of the cancer cells.[5−7] Cancer cells produce a high level of GSH and antioxidants, which increases their survivability against several chemotherapeutic drugs.[8,9] However, there are currently no proven methods for attacking mitochondrial redox homeostasis. In some cases, intracellular ROS generated by nanomaterials are rapidly quenched by excess GSH present in cancer cells. Several bioactive peptides,[10] self-assembled nanoparticles,[11] and carbon-based materials[12] have recently been used to rapidly conjugate with GSH via electrophilic−nucleophilic or ionic interactions, thereby inactivating the GSH before it reaches mitochondria.[2] Moreover, some of those nanomaterials could trigger nitric oxide (NO) production in mitochondria, which induces the synthesis of several apoptotic factors.[13] In addition to targeting mitochondria, recent strategies have also been employed to target the DNA of cancer cells. During DNA replication, the helicase enzyme unwinds double-stranded DNA to generate single-stranded DNA. At this time, the nucleus is more vulnerable to various chemotherapeutic drugs and nano-

Received: May 26, 2023
Revised: September 28, 2023
Accepted: October 2, 2023
Published: October 31, 2023

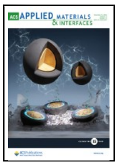

ACS Publications © 2023 American Chemical Society

https://doi.org/10.1021/acsami.3c07547

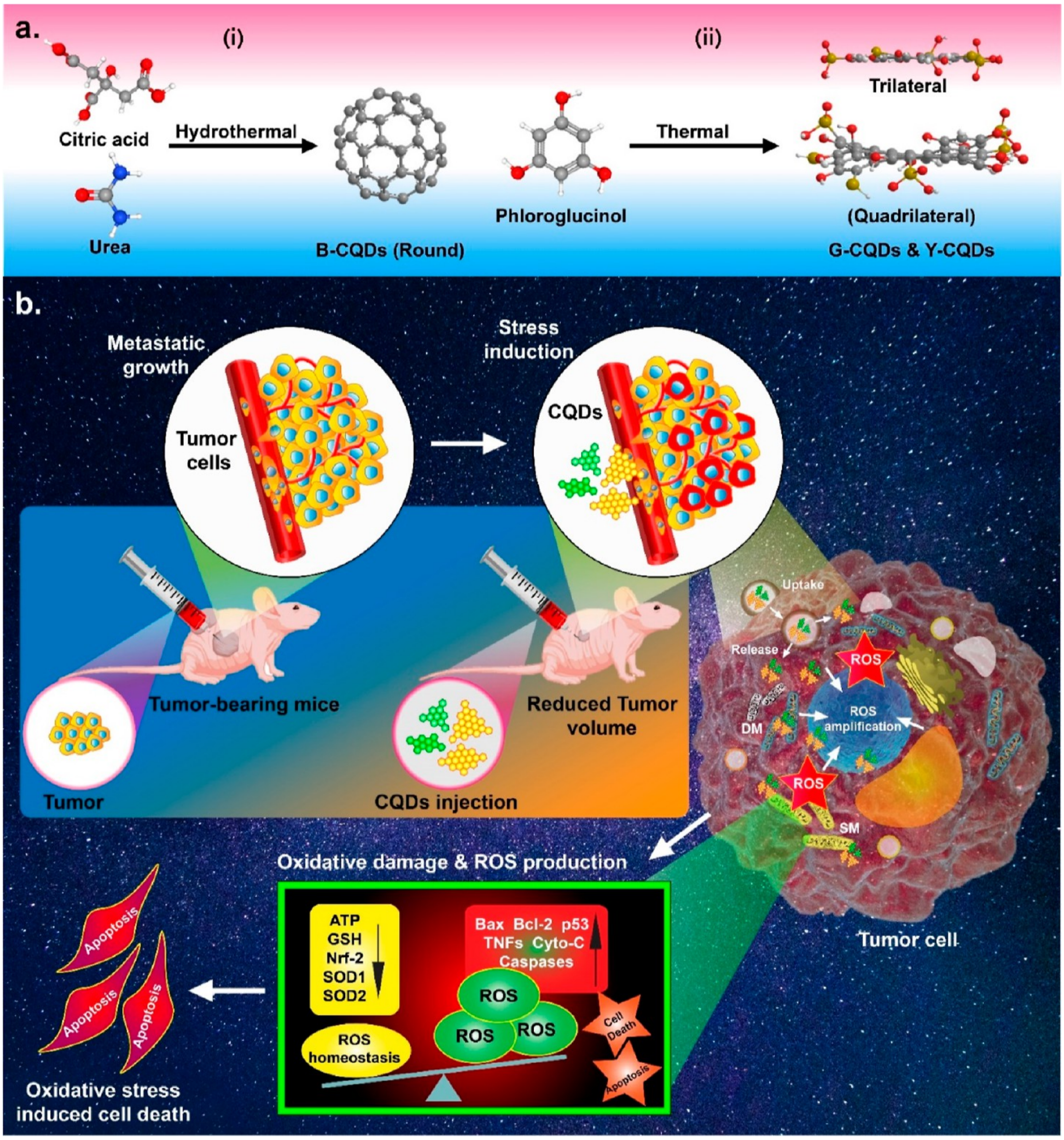

Figure 1. (a) Schematic diagram for CQD preparation, and (b) CQD-induced mitochondrial stress response and enhanced anticancer activity for solid tumors. DM, damaged mitochondria and SM, stressed mitochondria.

particles. As a result, various nucleus-targeting molecules have been designed to enhance cancer therapy by the local delivery of drugs.[13,14] We suggest that to achieve an effective treatment a combined strategy is needed to target both the mitochondria and nucleus by synergistically elevating ROS levels and DNA damage in cancer cells.

Recently, various nanomaterials have been extensively used for cancer therapy that counters the significant drawbacks of traditional chemotherapy-based treatments.[15] The nanoparticle-based tumor targeting strategies are unsatisfactory due to the higher organ toxicity, less accumulation in the tumor site, and insufficiently produced ROS that induces apoptotic cell death.[16,17] To some extent, drug-conjugated nanoparticles exhibit severe toxicity to normal cells and are a potential cause for cardiotoxicity and nephrotoxicity.[18] Recent studies indicate that carbon-based nanostructured materials, such as bright and photostable carbon quantum dots (CQDs) with size-tunable fluorescence properties, have gained significant attention in the biomedical field.[19,20] The nanoscale size and tailorable surface functionalities of CQDs make them suitable for use in bioimaging, biosensing, photocatalysis, and even in cancer theranostics.[14,21−23] The CQDs can be functionalized by the addition of various hydrophilic moieties to increase the water solubility and cellular uptake for targeting and biomolecular sensing. Several reports have demonstrated that CQDs act as mitochondrial stress amplifiers and DNA damaging agents. Metal ion-doped CQDs, containing ions, such as Cu^{2+}, Zn^{2+}, and Ni^{2+}, have been shown to have excellent tumor targeting and DNA damaging activity and have been reported to cause conformational changes in the DNA structure.[24] Moreover, CQDs supported with gold nanoparticles (CQD/AuNPs) have been previously demonstrated as mitochondrial ROS targeting agents (such as MitoCAT-g) in an orthotropic PDX tumor model.[2] Recently, Qi et al. engineered CQDs with the addition of folic acid (FA) for selective targeting of DNA in HeLa cells.[13] However, the potential application of AuNPs or FAmodified CQDs is hindered by the side reactions with biological fluids and organ toxicity.[25] Nevertheless, these CQDs alone cannot support both mitochondrial targeting and DNA cleavage activity. So far, the potential anticancer properties of CQDs of various shapes and sizes have not been explored.

In this study, we prepared polychromatic shape-engineered CQDs, from two different routes with excellent bioimaging properties (Figure 1a) and evaluated their antitumor efficacy in an in vivo tumor model. Blue emissive spherical carbon dots (B-CQDs) were synthesized using a well-known precursor via a conventional hydrothermal method. The polyphenol containing green-yellow emissive CQDs of specific shape (trilateral and quadrilateral) were synthesized using phloroglucinol, through the dehydration-induced ring fusion method, as reported earlier.[21] In our previous study, we examined the antitumor property of the G-CQDs via doxorubicin (DOX) loading and investigated the synergistic effects.[78] Thus, the present study focused on a comparative analysis of the three different CQDs with various physicochemical properties for drug-free tumor therapy. Interestingly, polyphenolic trilateral and quadrilateral G-CQDs alone have enhanced mitochondrial dysfunction by increasing the ROS levels and inducing DNA cleavage processes in melanoma cells (Figure 1b) and exhibited adequate in vivo biocompatibility. Moreover, the G-CQDs were found to localize in the mitochondria and amplify the stress response toward apoptotic cell death. The G-CQDs were also found to generate abundant $^\bullet OH^-$ and $^1O_2^-$ radicals under the acidic pH environment of cancer cells. Furthermore, the CQDs showed excellent photostability and two-photon (TP) bioimaging properties in cancer cells. Our results demonstrated that shape-engineered polyphenolic CQDs can significantly augment the treatment strategy of solid tumors with a superior imaging ability.

2. EXPERIMENTAL SECTION

2.1. Synthesis of CQDs. A simple one-step hydrothermal approach was employed to create the spherical CQDs with blue emission from the extensively used and generally accessible precursors citric acid and urea.[26] The motivation to synthesize shape-engineered CQDs was inspired according to the previous work reported by Yuan et al.[27] Shape-engineered CQDs (trilateral and quadrilateral) were synthesized according to our previous reports with a slight modification.[21] The details of the CQD characterization is reported in our previous study.[78]

The structural features and energy levels of the molecular orbitals of as-prepared CQDs were calculated through density function theory (DFT) calculations by the molecular mechanics (MM2) method. The optimized geometries of the CQDs were represented along with the predicted chemical structures, as shown in Figures S7 and S8.

2.2. In Vitro Studies. *2.2.1. Cell Lines.* B16F10 (KCLB no. 80008) and RBL2H3 (KCLB no. 22256) were purchased from KCLB Seoul National University, Republic of Korea. hBMSCs (ATCC-PCS-500-012) and hDFs (ATCC-PCS-201-012) were purchased from American Type Culture Collection, USA. RBL2H3 (passage 4), B16F10 (passage 4), and hBMSCs (passage 5) were cultured in DMEM media with a 10% heat-inactivated fetal bovine serum (FBS; Merck, USA) and 1% antibiotics (Gibco-BRL, USA) containing streptomycin (1000 μg/mL) and penicillin (10,000 U/mL) at 37 °C with 5% CO_2.

2.2.2. Bioimaging and Photostability Study. For one-photon (OP) bioimaging, the cells (2×10^4/well) were seeded in 35 mm confocal dishes and were treated with each CQDs (50 μg mL^{-1}). After 24 and 48 h intervals, the cell surface was washed with PBS to remove the unbounded CQDs. The OP imaging was captured by a confocal microscope (LSM 980 A-2, Zeiss, Germany) equipped with a live-cell imaging-incubator system at 37 °C and 5% CO_2. Images were captured with a 405 nm diode laser (30 mW, blue), 488 nm MAr laser (25 mW, green), and 561 nm DPSS laser (20 mW, red) light, and corresponding z-stack images were also taken. All the images were processed by ZEN software (Zeiss, Germany) and ImageJ Fiji plugins (www.imagej.nih.gov). FL images were also taken after 3 days of cell culture incubation with CQDs. The photostability experiment was conducted for up to 2 months using repeated imaging of stained B16F10 cells at different time points. The TP imaging was performed using a TCS SP5 II microscope (Leica, Germany). The TP sample preparation process and the colocalization study is described in our previous report.[78] Briefly, 50% confluent cells were coincubated of MitoTracker Red dye (0.5 μM, Life Technologies, USA) with G-CQDs for 30 min, 1 h, and 4 h, respectively. Next, the treated cells were fixed and permeabilized, and the colocalization process was photographed. The images were processed with Image Pro 6.0 software (Leica, Germany) and the colocalization threshold and Pearson's correlation coefficient (PCC) were calculated using ImageJ Fiji plugins.

2.2.3. Electron Spin Resonance Spectroscopy. To evaluate the ROS type generated by the CQDs, electron spin resonance (ESR) spectroscopy measurements were conducted by using DMPO or TEMP (Sigma-Aldrich, USA) as a spin trapping agent. The CQDs (20 μL) with the desired concentration were mixed with 0.5 mM H_2O_2 and 20 μL of 1 mM DMPO or TEMP before ESR measurements. After that, the solutions were gently mixed together and scanned for $^\bullet OH^-$ and $^1O_2$ radicals. All the experiments were conducted in dark conditions.

2.2.4. Detection of Hydroxyl ($^\bullet$OH) Radicals. The hydroxyl ($^\bullet$OH) radical generation potential of the CQDs was also measured using a commonly known fluorescence probe known as terephthalic acid (TA). For a typical reaction, the CQD-treated B16F10 and HDF cells (1×10^4 cells/well) were incubated with 0.5 mM TA and 20 mM H_2O_2. After that, the plates were immediately subjected to fluoresce measurement using a fluorescence spectrometer. A typical peak at 440−450 nm was considered as the formation of hydroxy TA.

2.2.5. Measurement of Cellular Oxidative Stress. The intracellular ROS level is evaluated by DCF-DA staining. H_2DCF-DA is a mitochondria-sensitive dye that is deacetylated by mitochondrial esterase to form a green fluorescent DCF or 2′,7′ dichlorodihydrofluorescein. The ROS level is measured by both microscopy and fluorometer. The cells were cultured for up to 5 days and incubated with specific concentrations of CQDs. The H_2DCF-DA (10 mM stock) was dissolved in methanol and mixed in DMEM to achieve a working concentration of 100 μM working solution. Following that, cells were treated with 100 μL of H_2DCF-DA at 37 °C for 30 min. The intracellular ROS was then seen using a fluorescence microscope at 485/520 nm excitation/emission after the cells had been washed with PBS. The cells were exposed to 40 μM H_2DCF-DA at 37 °C for 30 min prior to flow cytometry. A FACSCalibur flow cytometer (BD Biosciences, San Jose, USA) with an excitation wavelength of 488 nm and an emission wavelength of 530/585 nm filters was used to analyze stained cells. Dox (200 μM)- and H_2O_2 (200 μM)-treated cells were taken as the positive control.

2.2.6. DNA Damage and Cell Cycle Distribution Study. The CQD-induced DNA damage was monitored by an APO-BrdU Tunel assay kit (A23210, Thermo Fischer Scientific, USA) as reported in our previous study.[78] Briefly, the cells were incubated with B-CQDs (200 μg mL^{-1}), G-CQDs (100 μg mL^{-1}), and Y-CQDs (100 μg mL^{-1}) for 48 h and fixed with 0.1% PFA, digested by terminal deoxynucleotidyl transferase (TdT), and stained with AF-488 Anti-BrdU. Dox (200 μM)- and H_2O_2 (200 μM)-treated cells were taken as the positive control. The FL images were captured at 100 μm resolution, and Tunel-positive cells were counted by ImageJ software. Cell cycle analysis was carried out using propidium iodide (PI) staining as reported in our previous study.[28]

2.2.7. Mitochondrial Morphology Study. A Bio-TEM instrument was used to study the effect of different CQDs on the ultrastructure of mitochondria. Briefly, B16F10 cells were treated with B-CQDs (200 μg mL^{-1}), G-CQDs (100 μg mL^{-1}), and Y-CQDs (100 μg mL^{-1}) for

48 h. After specific treatment, the cells were fixed by fixation solution, sectioned, and observed under field-emission transmission electron microscopy (TEM) (JEM-2100F, Jeol, Japan) at different magnifications. Mitochondria of about 10 cells were analyzed for each treatment group.

The relative mitochondrial perimeter (p) and area (a) were calculated using ImageJ software, and the form factor (F) was calculated by following eq 1.[2]

$$\text{Form factor } (F) = \frac{4 \times \pi a}{p^2} \tag{1}$$

2.2.8. Cellular GSH and ATP Levels. The B16F10 cells were treated with B-CQDs (200 μg mL^{-1}), G-CQDs (100 μg mL^{-1}), and Y-CQDs (100 μg mL^{-1}) for 48 h. After that, the cells were trypsinized and lysed by RIPA buffer at 4 °C for 1 h. Next, the cell lysates were centrifuged at 11,000 rpm for 10 min, and the supernatant obtained was subsequently used for GSH measurements. A volume of 0.2 mL of lysates was mixed with freshly prepared 1 mL of 0.5 mM Ellman's reagent (5,5-dithio-bis-2-nitrobenzoic acid) and incubated for 5 min. After 5 min, the GSH activity was determined by measuring the absorbance at 405 nm. For mitochondrial GSH measurements, mitochondria were extracted by a mitochondria isolation kit (ab110170). The total ATP content was measured with an ATP assay kit (ab83355, Abcam, USA).

2.2.9. Mitochondrial Oxygen Consumption. Oxygen consumption rate (OCR) in B16F10 cells was measured by using an extracellular O_2 consumption kit (ab197243). The cells (4×10^4 cells) were treated with B-CQDs (200 μg mL^{-1}), G-CQDs (100 μg mL^{-1}), and Y-CQDs (100 μg mL^{-1}). At this point, 10 μL of the OCR reagent was added to each well and sealed by 100 μL of mineral oil. After a specific time, the OCR was analyzed using a fluorescence plate reader at Ex/Em of 380/650 nm, respectively. The OCR was calculated and compared with the control groups. Dox (200 μM)- and H_2O_2 (200 μM)-treated cells were taken as the positive control.

2.2.10. Detection of Apoptosis-Related Proteins. For in vitro detection of apoptotic proteins, B16F10 cells were cultured in a DMEM medium containing CQDs for 48 h. After 48 h, the cells were fixed and blocked by using standard protocols. After that, the cells were incubated with caspase-3 (sc-7272, SCBT, USA, 1:250) and cytochrome-C (sc-13560, SCBT, USA, 1:250) primary and secondary antibodies (SCBT, USA, 1:500), followed by staining with Cy3 dye (Thermo Fischer Scientific, USA). After desirable antibody labeling, the cells were visualized by an inverted fluorescence microscope (DMi8, Leica, Germany). About 20 cells were counted from each microscopic field and are subsequently used for quantitative analysis. Total protein lysates were analyzed by an Apoptosis Array C1 kit (AAH-APO-1-8, RayBiotech, USA), and the protein spots were quantified by ImageJ software.

2.2.11. qRT-PCR Analysis. The apoptotic gene marker expression was assessed using qRT-PCR analysis. For this, total RNA was isolated from B16F10 cells following CQD treatment by the RNAzol RT reagent (Sigma-Aldrich, USA). The cDNA synthesis was carried out using 2 μg of total RNA by the superscript II RTase enzyme (Invitrogen, MD, USA) in a thermocycler. Next, the purified cDNA was used for qRT-PCR analysis as described previously.[29] The qRT-PCR reaction was carried out using a CFX96 Maestro Real-Time system (Bio-Rad, USA). The primer sets (Bioneer Corp., Daejeon, Republic of Korea) and their sequences are given in Table S1.

2.2.12. Cell Proliferation Assays. The antiproliferative property of the CQDs was investigated using a WST-1 assay. Briefly, cells (1×10^4/well) were treated with CQDs (0, 25, 50, 75, 100, 125, 150, and 200 μg mL^{-1}) for 48 h. Plates treated with Dox (200 μM) and H_2O_2 (200 μM) were considered to be positive controls. The cells were treated with 10 μL of WST-1 dye and then incubated for 2 h after a predetermined interval. The absorbance was measured at 450 nm, and data were normalized with control groups. For the colony formation assay, the CQDs-treated B16F10 cells were stained with 0.5% crystal violet. Sainted colonies were captured by a digital camera (Sony Cybershot, DSC-W380).

2.2.13. In Vitro Migration and Invasion Assays. The cells were cultured with B-CQDs (200 μg mL^{-1}), G-CQDs (100 μg mL^{-1}), and Y-CQDs (100 μg mL^{-1}) in transwell migration and invasion chambers using 8 μm inserts (Corning, USA). The cells were serum-starved for 12 h. After specific time intervals, the cells were subsequently fixed by 3.7% PFA, permeabilized by absolute methanol and Giemsa stained. After staining, the insets were washed thrice by sterile D.W. and were photographed. ImageJ counted the number of migrated cells. For the invasion study, the fixed cells were additionally stained by DAPI (Sigma-Aldrich, USA).

2.3. In Vivo Studies. *2.3.1. Hemocompatibility.* For the hemocompatibility test, blood samples were collected from healthy mice. The RBCs were extracted from the whole blood, as reported earlier[2] The RBCs were washed several times with PBS until the supernatant was colorless. 6× diluted RBCs (in PBS) were mixed with B-CQDs (200 μg mL^{-1}), G-CQDs (100 μg mL^{-1}), and Y-CQDs (100 μg mL^{-1}) and incubated for 120 min at 37 °C. After incubation, the blood samples were centrifuged at 1000 rpm for 5 min to spin down the RBCs. A volume of about 100 μL of supernatant was collected from each tube, and the absorbance (Ab) was measured at 540 nm as a spectrum for hemoglobin. The percentage of hemolysis was calculated by following eq 2

$$\text{Hemolysis } (\%) = \frac{\text{Ab}_\text{T} - \text{Ab}_\text{NC}}{\text{Ab}_\text{PC} - \text{Ab}_\text{NC}} \times 100 \tag{2}$$

where, Ab_T, Ab_NC, and Ab_PC indicate the treatment, negative control, and positive control, respectively.

2.3.2. Animals for In Vivo Study. BalB/c nude mice (female, 4–6 weeks old) were received from Beijing HFK Biosciences Co. Ltd. and raised in a pathogen-free environment. The Institutional Animal Care and Use Committee (IACUC) of the Institutional Review Board (IRB), Capital Medical University Hospital, China, granted permission for the animal research to be carried out (CMUSH-IRB-KJ-2020-29).

2.3.3. Ex Vivo Biodistribution Analysis. All animal experiments were approved by the Capital Medical University Hospital, China. 4–5 week old BALB/c mice were used for the biodistribution study. The mice were given free access to mouse food and water during experiments. The ex vivo organ imaging was performed as reported in our previous study.[78]

2.3.4. Subcutaneous Tumor Model and In Vivo Therapeutic Efficacy of CQDs. The right flank of the BalB/c nude mice received a subcutaneous injection of around 2 105 B16F10 (200 μL) cells. Five groups ($N = 5$) of five mice each (a total of 25 animals) were used to conduct the experiment. Every second day, seven intratumoral injections of the different CQD formulations: 200 g mL^{-1} (B-CQDs) and 100 g mL^{-1} (G-CQDs and Y-CQDs) were given to each animal. The dosage for the Dox-treated (positive control) group was 5 mg kg^{-1}. The groups that received PBS were used as the adverse control. The tumor volume was calculated using following eq 3

$$\text{Tumor volume } (V) = \text{Tumor length } (L) \times \text{Width } (W^2) \times 1/2 \tag{3}$$

After 25 days of treatment, all the mice from different groups were sacrificed, and the therapeutic efficiency of CQDs has investigated through hematoxylin and eosin (H&E) staining.

2.4. Statistical Analysis. Origin Pro v9.0 (Origin Laboratories, USA) was used for the statistical analysis, and all results are the mean ± standard deviation of three replicated trials ($n = 3$). The one-way ANOVA test and the Student's t-test were used to conduct the statistical analysis. Box plots in the in vitro experiments indicate the maximum and minimum variations in data sampling during experiments. Statistical significance was considered at $*p < 0.05$. The in vivo survivability test was conducted using the Kaplan–Meier survival test, and the p-values were selected from the log-rank test.

3. RESULTS AND DISCUSSION

Spherical CQDs were obtained via polymerization of urea and citric acid at high temperatures, as shown in Figure S1a. The

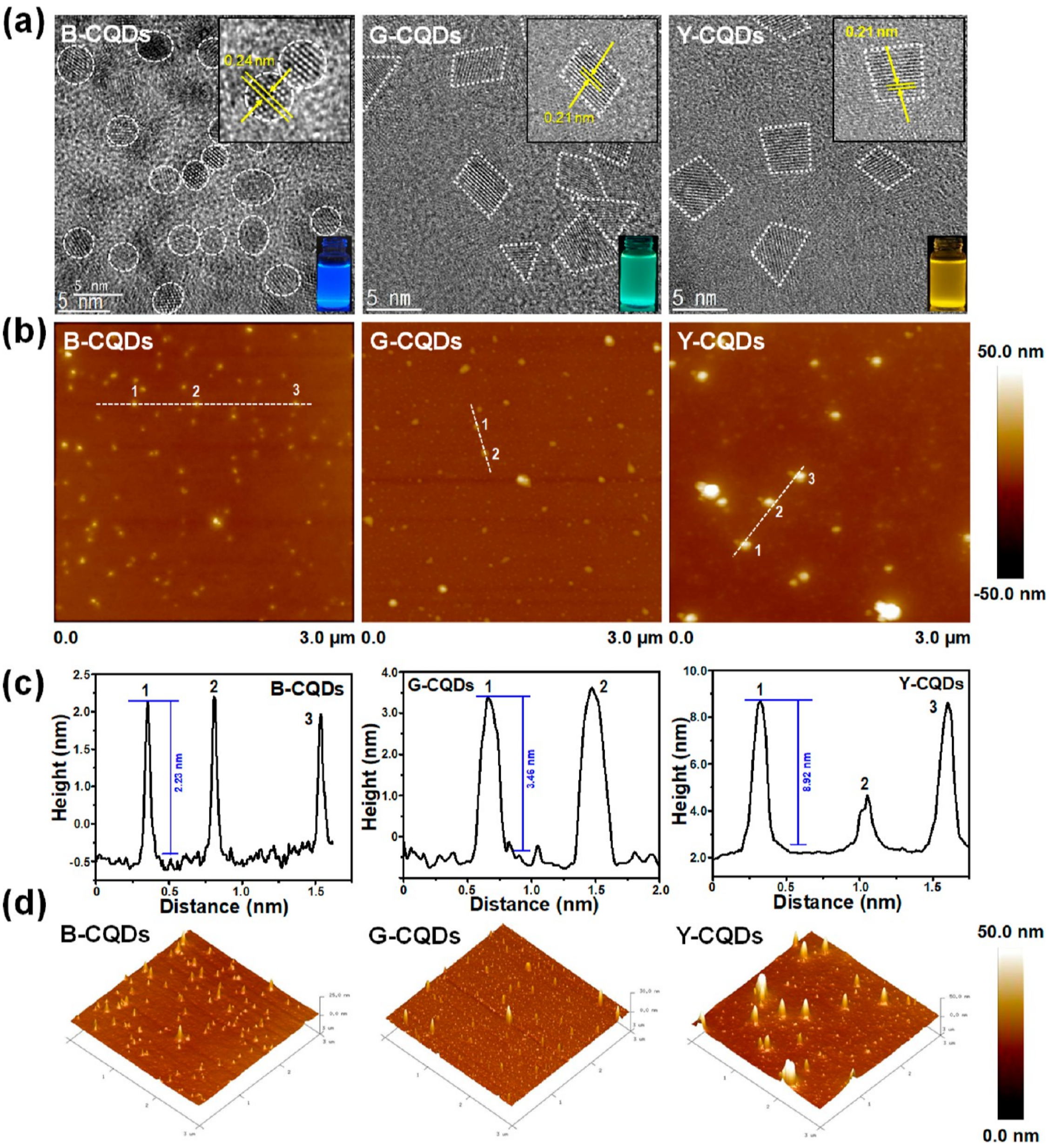

Figure 2. Morphology of the CQDs. (a) HR-TEM images of CQDs at different magnifications. The insets showed liquid-state fluorescence images of the CQDs. Scale bar: 5 nm (b) AFM images with corresponding (c) 2D and (d) 3D height profiles of B-CQDs, G-CQDs, and Y-CQDs. Scale bar: 50 nm and 3 μm.

condensation polymerization leads to the formation of polymer-like materials, which further carbonize at high temperatures to form spherical-shaped CQDs.[26] Subsequently, the shape-engineered CQDs (trilateral and quadrilateral) with discernible edge structures were synthesized using phloroglucinol.[21,27] The selection of phloroglucinol, a triangulogen compound with a distinctive molecular symmetry and three reactive protons that are activated by three electron-donating hydroxyl (−OH) groups, was made after careful consideration. During thermal synthesis, several phloroglucinol molecules undergo ring cyclization through the removal of −H and −OH groups in the sulfuric acid medium, as shown in Figure S1b. Photographs of the purified and highly crystalline CQDs are shown in Figure S2. The CQD formation mechanism was studied using NMR spectroscopy. ^{1}H NMR spectra (Figure S3a) of B-CQDs showed several peaks around $\delta = 1{-}4$ ppm, corresponding to the protons connected to carbon with an electronegative atoms (oxygen and nitrogen) or carbonyl residues nearby.[30] The small peak around $\delta = 6.0$ ppm may be attributed to the HC═ group. ^{1}H NMR spectra (Figure S3b,c) of G- and Y-CQDs consist of various peaks within 7.3−7.6 ppm, indicating the fusion of several phloroglucinol molecules to form a large polyaromatic CQD framework. Numerous signals around 6.5−6.9 ppm indicate the presence of −H of −OH and −SH/SO_3H groups. ^{13}C NMR spectra of B-CQDs (Figure S3d) exhibited several peaks at 20−70 ppm, corresponding to sp^3 carbons attached to electronegative atoms (O and N) or C═O and C═N groups. Peaks detected at approximately 100 ppm were due to the presence of C═C groups, and 150−185 ppm were detected for −COOH, −$CONH_2$, and C═N groups. ^{13}C NMR spectra of the G- and Y-CQDs (Figure S3e,f) consist of several peaks between 143 and 165 ppm due to the sp^2=hybridized carbons connected to −OH groups at the surface. Moreover, numerous peaks

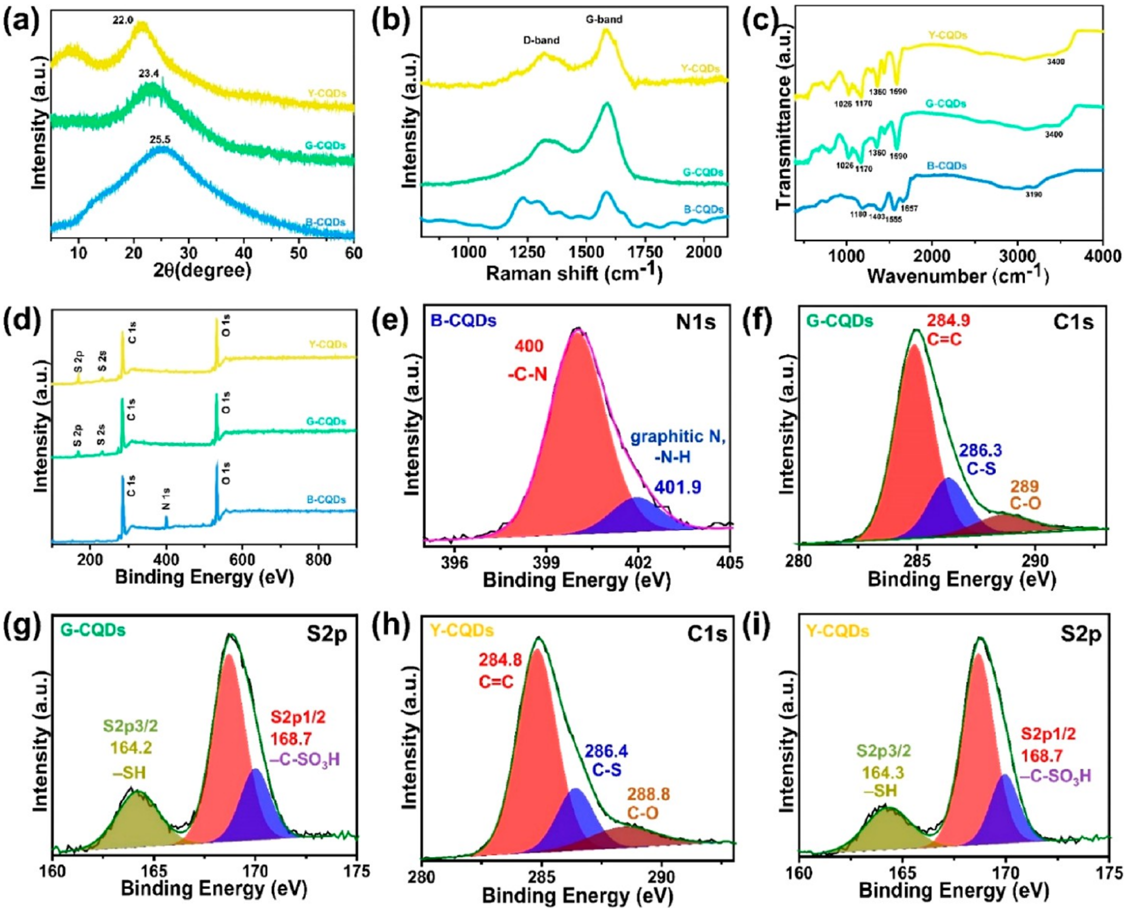

Figure 3. Characterization of the CQDs. (a) XRD patterns, (b) Raman spectra, (c) FT-IR spectra, and (d) XPS total survey spectra of the CQDs. High-resolution XPS spectra of (e) B-CQDs, (f,g) G-CQDs, and (h,i) Y-CQDs.

between 114 and 140 ppm also reflect the synthesis of compact large sp^2 polyphenolic structures. The ζ potentials of the B-CQDs, G-CQDs, and Y-CQDs were measured to be −16.03, −32.4, and −42.96, respectively (Figure S4). It is likely that the presence of groups with stronger electronegative properties is responsible for the higher ζ potentials of G-CQDs and Y-CQDs.

For detailed structural and morphological analysis, high-resolution TEM (HR-TEM), atomic force microscopy (AFM), X-ray diffraction (XRD), and Raman spectroscopy were conducted. The TEM images of B-CQDs (Figure 2a) showed a spherical morphology of crystalline carbon nanodots with diameters of approximately 3−6 nm having a lattice spacing around 0.24 nm.[26] The TEM images of the polyphenol containing CQDs exhibited unique crystalline structures of trilateral/quadrilateral particles, with a size distribution of 4−8 and 5−10 nm for G- and Y-CQDs with a unique crystal spacing around 0.21 nm, respectively.[21] The TEM images of the polyphenol containing CQDs exhibited a lattice spacing of 0.22 nm, indicating the interplanar spacing of the (100) plane, which corresponds to a defect-free graphene morphology.[27,31] TEM with a corresponding fast Fourier transform (FFT) pattern of repeat data ($n = 2$) is shown in Figure S5. The TEM images exhibited similar structural features as-obtained in the first batch of synthesis conferring the definite shape of the CQDs. The AFM images with the corresponding thickness and 2D and 3D height profiles of B-CQDs, G-CQDs, and Y-CQDs are presented in Figure 2b−d. The average heights of the B-CQDs, G-CQDs, and Y-CQDs were 2.23, 3.46, and 8.92 nm, which also resembles the TEM data. The average thickness of the B-CQDs, G-CQDs, and Y-CQDs were found to be 2.23, 3.46, and 8.92 nm corresponding to the unique graphene or graphene oxide-like structure of CQDs.[27] The XRD spectra (Figure 3a) of the B-CQDs showed a broad diffraction peak located at $2\theta = 25.6°$, indicating a highly disordered carbon structure.[26,32,33] The XRD patterns of the G- and Y-CQDs also displayed peaks corresponding to the (001) facet located at 23.4 and 22.0°, respectively. The narrowness of the Y-CQD XRD compared to the XRD of the G-CQDs indicates a larger conjugated domain and crystalline nature of the Y-CQDs.[27] This was further explained by the crystallite size of the particle by using the Scherrer equation (Table 1). It is interesting to note that the average crystallite sizes for B-CQDs, G-CQDs, and Y-CQDs were calculated to be 4.36 (fwhm: 18.3), 7.1 (fwhm: 11.4), and 10.2 (fwhm: 7.8) nm, which are in good accordance with the HR-TEM and AFM results (Figure S6). The Raman spectra (Figure 3b) of the CQDs were recorded to investigate the intrinsic structure. The Raman spectra of the B-

Table 1. Average Size of the Crystallite or Particle of the CQDs Derived from the Scherrer Equation

sample	peak position (2θ)	fwhm (2θ)	crystallite size (nm)
B-CQDs	25.6	18.3	4.36
G-CQDs	23.4	11.4	7.1
Y-CQDs	22	7.8	10.2

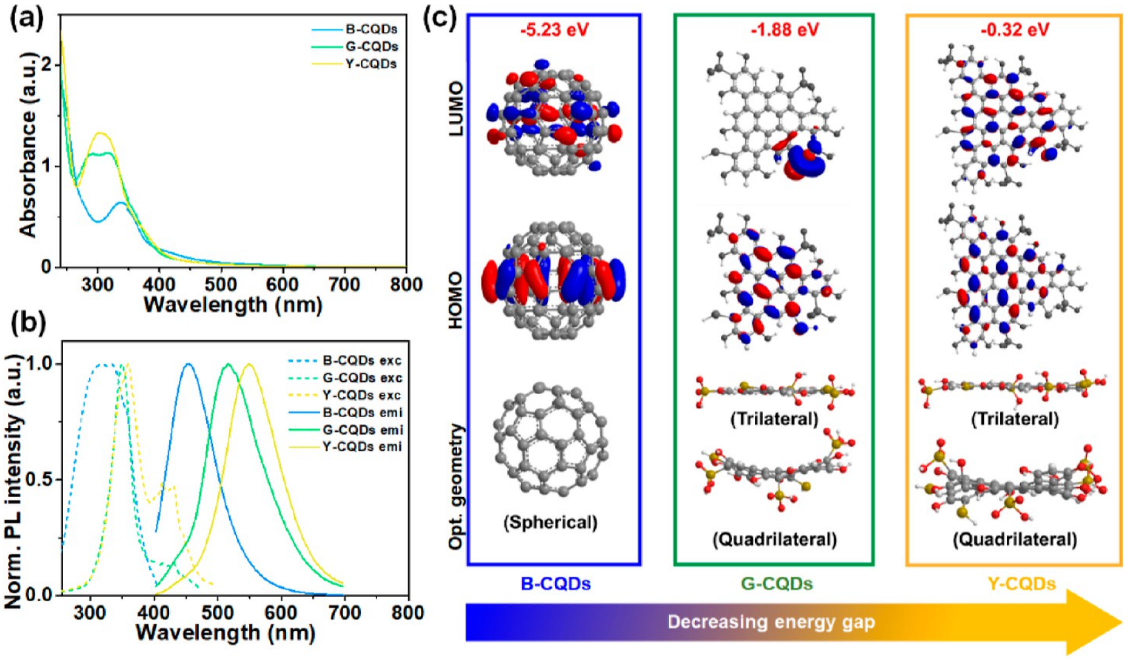

Figure 4. Optical properties of the shape-engineered CQDs. (a) UV−vis absorption spectra of the CQDs. (b) PL excitation (dotted-line) and PL emission (solid-line) spectra of the CQDs (0.1 mg mL^{-1} each). The excitation wavelength for B-CQDs, G-CQDs, and Y-CQDs are 320, 350, and 355 nm, respectively. (c) LUMO and HOMO configuration of B-CQDs, G-CQDs, and Y-CQDs were represented with the corresponding optimized geometries as predicted through the MM2 method.

CQDs showed a peak at around 1250 cm^{-1} due to the C−C (Sp^3 carbon) and C−O groups. The typical spectra at 1590 cm^{-1} attributes to the G-band, which signifies the sp^2-conjugated carbons. The Raman spectra of the G- and Y-CQDs exhibited two peaks at approximately 1340 and 1590 cm^{-1}, indicating the D- and G-bands, respectively. The (I_G/I_D) value for G- and Y-CQDs compared to B-CQDs indicates the synthesis of highly crystalline graphitic CQDs, which is in accordance with our previous report.[78]

In addition, the chemical compositions of the CQDs were examined by using FT-IR and XPS analyses. As presented in Figure 3c, the B-CQDs FT-IR spectra showed peaks around 1403−1180 and 1657−1555 cm^{-1} due to the C−N/C−O stretching and C═N/C═O groups, respectively. The peaks in between 1403 and 1657 cm^{-1} signify the existence of CN heterocycles in the CQD domain.[34] In addition, the peaks located around 3190 and 3400 cm^{-1} are attributed to N−H and O−H groups. Interestingly, FT-IR spectra of the polyphenolic CQDs contain C−O/C−S and O−H groups at approximately 1170 and 3400 cm^{-1}. The peak at 1590 cm^{-1} was due to the presence C═C bonds of the polyphenolic CQDs, containing hydroxyl groups at the surfaces.[35,36] The presence of the sulfonyl group ($-SO_3H$) was observed in between 1360 and 1026 cm^{-1}, which implies that polyphenolic carbon structures were mainly composed of −OH and $-SO_3H$ groups on the edges.[37] The XPS total survey spectra (Figure 3d) of B-CQDs displayed 285.2, 400.5, and 532.9 eV corresponding to the C 1s, O 1s, and N 1s regions. The XPS spectra of the polyphenolic CQDs are also composed of three elements, as confirmed by the presence of S 2p, C 1s, and O 1s. The high-resolution N 1s spectra of B-CQDs (Figure 3e) showed the presence of −C−N and graphitic N/N−H in the region of 400 and 401.9 eV. The C 1s XPS spectra of polyphenolic CQDs (Figure 3f,h) consist of three peaks at 284.9, 286.4, and 289 eV, which implies the presence of C═C, C−S, and C−O bonds. The S 2p XPS spectra of the polyphenolic CQDs (Figure 3gi) reflected two peaks at 164.3 and 168.7 eV owing to the presence of −SH or S $2p_{3/2}$ of sulfonic group and S $2p_{1/2}$ of sulfonic acid group ($C-SO_3H$), respectively. The optical characteristics of polyphenolic CQDs are primarily determined by the quantum confinement effect, which is influenced by the size of the CQDs. This effect is shown by the similar chemical bonding, elemental composition, and valence states seen in the CQDs, rather than the surface states. Moreover, the O 1s spectra of B-CQDs exhibited peaks around 532.28, 531.30, and 533.74 eV correspond to the oxygen bonded with carbon atoms (C−O−H/C═O/C−O−C) (Figure S7a), whereas the polyphenolic CQDs exhibited nearly similar peaks around 533 eV and 531 and 534 eV related to the oxygen bound to the carbon (C−O−H/O−C═O) and sulfur (S═O or S−O), respectively (Figure S7b,c). Thus, based on the spectroscopic analysis, it was revealed that B-CQDs mostly exhibit −O−H, N−H, C═C/C═N, and, C−C/C−N bonds, whereas, the polyphenolic CQDs are made up of C═C, C−O, C−S, −SH, and $-C-SO_3H$ surface charges. Our results showed that B-CQDs are amorphous in nature, with a spherical morphology, while G- and Y-CQDs have a polyaromatic crystalline trilateral/quadrilateral morphology with −OH and $-SO_3H$/−SH functional groups on the edges.

To further inspect the luminescent properties of the CQDs, UV−vis spectra (Figure 4a) were recorded. We have observed a broad peak around 338 nm for B-CQDs, indicating the $n-\pi^*$ transition of −O/−N-containing groups.[26] The polyphenolic CQDs exhibited peaks at 289 and 305 nm in ethanol, respectively, corresponding to the $\pi-\pi^*$ transition of conjugated benzene/phenolic rings. The PL spectra displayed emission peaks at 453 nm for B-CQDs, corresponding to blue emission, while the emission peaks of the polyphenolic CQDs were centered at 516 nm (green emission) and 550 nm (yellow

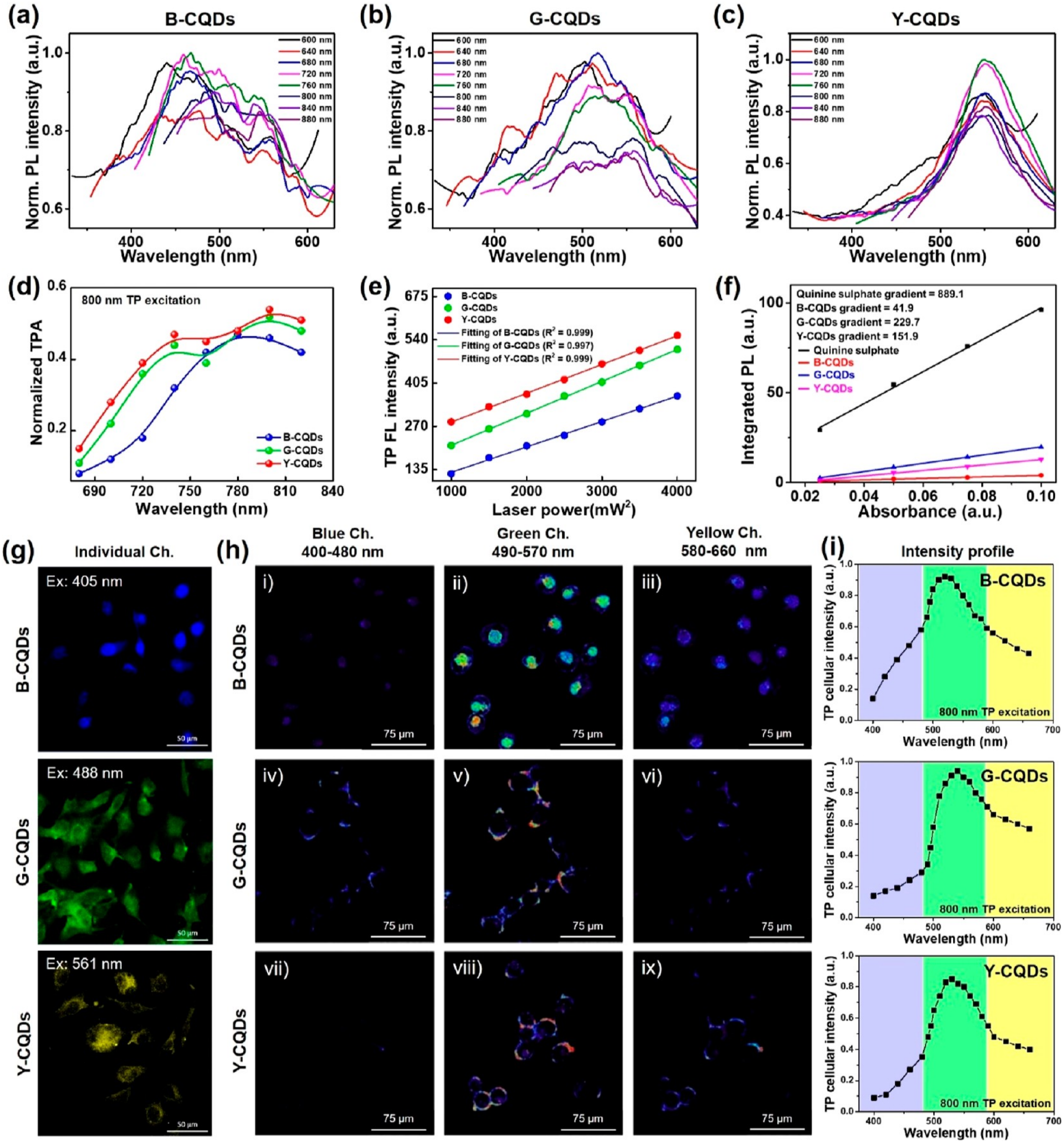

Figure 5. (a−c) Representative TP emission spectra of the CQDs (0.1 mg mL^{-1} each) upon excitation of 600−800 nm. (d) Normalized TPA spectra of the CQDs at 600−800 nm excitation. (e) Relationship between TP emission intensity and the square of laser power density. (f) FL quantum yield (QY) measurement of the CQDs. Quinine sulfate was taken as the control. (g) OP bioimaging of B16F10 cells treated with various CQDs (50 μg mL^{-1} each). Scale bar: 50 μm. (h) TP bioimaging of B16F10 cells after B-CQDs (i−iii), G-CQDs (iv−vi), and Y-CQDs (vii−ix) treatment. Scale bar: 75 μm. (i) TP cellular intensity of individual cells after CQDs treatment under 800 nm TP excitation.

emission), respectively (Figure 4b). The excitation wavelength-dependent PL emission spectra also exhibited minor changes with maximal emission values observed at excitation wavelengths of 320 nm for B-CQDs, 350 nm for G-CQDs, and 355 nm for Y-CQDs (Figure S8).

To gain insights into the structural features and energy orbital distributions, we optimized the geometries using the MM2 method. We hypothesize that the luminescent features of the polyphenolic CQDs exhibit several fused benzene rings, consisting of either electron-donating hydroxyl groups (−OH) or electron-withdrawing sulfonyl groups (−SO_3H). The trilateral and quadrilateral structures of the CQDs, with possible surface functional groups, are presented in Figures S9 and S10. The trilateral geometries of G-CQD and Y-CQD were planar; however, quadrilateral geometries were puckered in shape. The HOMO−LUMO band gap energies are calculated and are exhibited in Figure S11. The HOMO−LUMO energy gap decreased as we moved from B-CQDs to Y-CQDs, which may justify their gradual bathochromic shift from 453 to 550 nm, respectively (Figure 4c). Remarkably, the

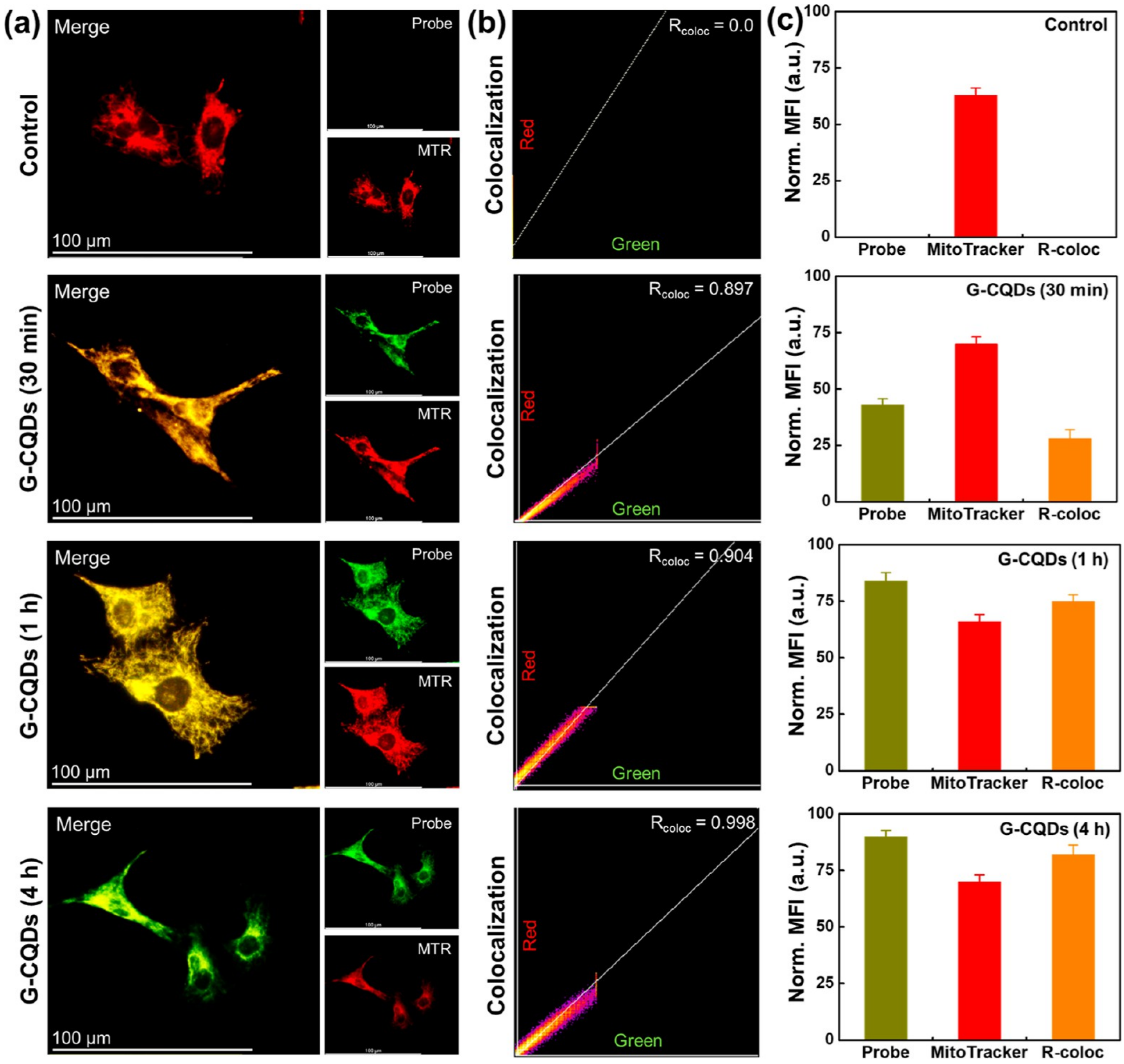

Figure 6. Mitochondria targeting ability of G-CQDs. (a) CLSM images with corresponding probe (G-CQDs, green color, 50 μg mL^{-1}), MTR (MitoTracker Red, red color), and merge images of cells showing the coexistence of G-CQDs in the mitochondria. (b) Fluorescence colocalization analysis (red/green; 0−255 scale) of the FL images with corresponding (c) normalized mean fluorescence intensities (norm. MFI) of the B16F10 cells showing the colocalization of G-CQDs in the mitochondria. The images were taken at various time intervals (30 min to 4 h). Cells without G-CQD treatment were considered as the control. Scale bar: 100 μm.

predicted electron cloud densities for the HOMO and LUMO in all CQDs were uniformly distributed across the molecule structure in the CQDs. Therefore, theoretical studies conclusively show that triangular and quadrilateral geometries with pure hydroxyl groups that donate electrons are the most stable structures, possibly accounting for the developed CQDs' exceptional color purity.[27] Such unique CQDs could be used for tagging various bioactive molecules, including chemotherapeutic drugs for tumor therapy.[78]

Next, we performed a bioimaging assay using shape-engineered CQDs in B16F10 melanoma cells in vitro. The OP and TP cell imaging was conducted using a CLSM, coupled with either single or multiphoton femtosecond laser source. Before testing the TP bioimaging, the near-infrared (NIR)-responsive behavior of the CQDs was tested. In our previous study, we only demonstrated the bioimaging capabilities of the G-CQDs tagged with DOX.[78] Herein, we systemically characterized the bioimaging abilities of the three different CQDs with varying emission. Figure 5a−c shows that B-CQDs, G-CQDs, and Y-CQDs displayed fluorescence upconversion at wavelengths of 470−665 nm, signifying their NIR absorption capabilities. Furthermore, the relative maximum TPA rate of the CQDs was first estimated to be 800 nm (Figure 5d). Among the tested wavelengths, all the CQDs exhibited superior emission in the 700−800 nm range, which is in accordance with the PL data. Additionally, it was found that the TP emission intensity of the CQDs increased linearly with the square of laser power (Figure 5e), confirming the TP excitation process. It is well known that a large TPE cross-section results in greater bioimaging owing to the higher absorbed energy/input energy flux ratio in cells. Herein, the absolute TPE cross-section (σ) for B-, G-, and Y-CQDs were estimated to be around 21455.9, 43390.4, and 42577.3 GM (derived under 800 nm TP excitation taking rhodamine B as a standard) (Table S2). Next, we determined the QY of the CQDs to understand their optical nature. As shown in Figure

5f, the QYs of the B-, G-, and Y-CQDs were calculated to be 0.03, 0.15, and 0.10, relative to the standard reference (quinine sulfate in 0.1 M H_2SO_4). The greater TPE cross-section area and increased QY indicate the enhance TP-responsive properties of a fluorophore.[38] In this context, the G-CQDs with $\sigma = 43390.4$ GM and QY = 0.15 is expected to have better bioimaging property in vitro. In addition, a time-resolved OP measurement was performed to analyze the lifetime of the B-, G-, and Y-CQDs, which were found to be 5.86, 7.14, and 7.88 ns, respectively (Table S2). Thus, shorter lifetime and increased QY could possibly be the reason for excellent NIR-responsiveness of the polyphenolic CQDs owing to the sp^2-hybridized carbon atoms and delocalized electron clouds entering the π^* state, thereby increasing the TPE cross-section.[39] On the other hand, the TP emission of B-CQDs was due to the enhanced charge-transfer efficiency due to the large π-conjugated domain and strong electron-donation moieties of the N-doped B-CQDs. Moreover, the CQDs showed excellent dispersion stability under high salt concentration (150 mM NaCl), proteins, and even acidic pH, suggesting that the CQDs will be highly stable in biological fluids (Figure S12).

The OP bioimaging of B16F10 cells was performed using 50 μg mL^{-1} of CQD treatment, as selected through concentration-dependent imaging. Figure 5d represents the OP confocal imaging of B16F10 cells in different excitations (405, 488, and 561 nm) with the corresponding pseudocolor merge images. The mean fluorescence intensities of the B-, G-, and Y-CQD-treated cells are shown in Figure S13. The FL images obtained at $\lambda_{ex} = 405$ nm indicate that the B-CQDs predominantly agglomerate in the nucleus. However, the G-CQDs ($\lambda_{ex} = 488$ nm) and Y-CQDs ($\lambda_{ex} = 561$ nm) were localized mainly in the cytoplasmic region, leaving a clear zone in the nucleus. These results were confirmed by performing a procedure that consisted of incubating the cells for up to 72 h to demonstrate the potential of the prepared CQDs as bioimaging probes (Figure S14). The obtained results were similar to the observations reported earlier.[14,40,41] We used an 800 nm excitation laser for TP bioimaging because the emission intensity was greater at this wavelength. Figure 5e shows that B-CQDs are selectively localized in the nucleus with a maximum fluorescence emission signal at 490−570 nm, respectively. Besides, the polyphenol containing CQDs were primarily targeted to the membrane region with a maximum fluorescence signal at 490−570 nm. The amine-functionalized CDs have a higher affinity toward the nucleus due to their zwitterionic nature. The zwitterionic nature allows a higher colloidal stability in varying pH and resistance to nonspecific adsorption of proteins therefore ensures rapid binding with nucleic acids.[42,43] In contrast, the polyphenol-containing CQDs have a higher affinity toward other subcellular organelles. Therefore, the selective localization of the CQDs is not size-dependent and is due to the surface functionalities. Figure 5f−h shows the fluorescence intensities of B16F10 in the presence of CQDs. Therefore, the OP and TP cell imaging experiments confirmed the superior bioimaging property of the CQDs.

Next, photostability was conducted to evaluate the stability of the CQDs as a bioimaging probe. The B16F10 cells treated with G-CQDs showed higher photostability at room temperature for up to 2 months (Figure S15), which further demonstrates the great bioimaging potential of the CQDs. In our previous study, we showed the cytoplasmic and nuclear localization of the G-CQDs owing to the presence of DOX molecules.[78] However, the potential of G-CQDs to invade mitochondria was not elucidated. To investigate the mitochondria targeting property, we used the G-CQDs (50 μg mL^{-1}) based on the overall in vitro studies. The G-CQDs were coincubated with MitoTracker Red (0.5 μM) for various time intervals. To avoid the spectral overlap between G-CQDs and the dye, intensity-based pseudocolor merge images were prepared to understand the colocalization of the G-CQDs with MitoTracker dye. As shown in Figure 6a, the G-CQDs colocalized with MitoTracker dye as incubation time increased from 30 min to 4 h, respectively. The PCC was calculated and presented as the R_{coloc} value to measure the colocalization efficiency. Interestingly, the R_{coloc} value was higher as the incubation time increased, suggesting that G-CQDs sufficiently accumulated inside the mitochondria. The R_{coloc} value for 30 min and 1 and 4 h incubation was calculated to be 0.897, 0.904, and 0.998, respectively (Figure 6b), which is consistent with the previous reports.[44−46] The mean fluorescence intensities (MFU) of the G-CQDs, MitoTracker Red, and colocalized images are shown in Figure 6c. An intensity-based pseudocolor image of the G-CQD localization is shown in Figure S16. Therefore, we anticipate that the mitochondria targeting property of G-CQDs could be utilized for studying the mitochondrial-mediated cell death in cancer cells.

The in vitro anticancer properties of the CQDs were investigated through the WST-1 assay. The CQDs exhibited higher cytotoxicity at 100 μg mL^{-1} (G- and Y-CQDs) in B16F10 cells (Figure S17b,c). It is noteworthy that B-CQDs exhibited restricted cytotoxicity and induced a marginal reduction in viability at a concentration of 200 μg mL^{-1} (Figure S17a). This may be explained by low levels of oxidative stress in the cells, which make them less susceptible to mitochondria.[2] However, only ∼10−20% of cells were found viable after G- and Y-CQD treatment. A similar pattern of cytotoxicity in the presence of G-and Y-CQDs was also noted in hDFs (Figure S18). We also verified a decreased efficiency of colony formation of the B16F10 cells after polyphenol containing CQD treatment, comparable to that of the Dox (200 μM)-treated groups (Figure S19). This is due to the high ROS amplification by mitochondria in the B16F10 cells, which is consistent with previous reports.[25,47] The toxicity of the graphene-like CQDs is likely to be caused by the activation of several endoperoxidases, leading to the generation of mitochondrial ROS.[19,48−50] The lethal effect of the CQDs was also investigated by in vitro migration and invasion assays. As presented in Figure S20, reduced cell migration was noted when the B16F10 cells were exposed to a lethal dose of the CQDs. Similarly, cell invasion properties were drastically changed after CQD treatment, indicating that shape-engineered polyphenol-containing CQDs have higher cytotoxicity, as documented in Figure S21.

The effects of shape-engineered CQDs on ROS amplification and nucleic acid damage were investigated by CLSM using the DCFH-DA and the TUNEL staining assays. As shown in Figure S22a, H_2O_2 (200 μM)- and Dox (200 μM)-treated cells exhibited high ROS levels after 48 h of incubation, compared to the PBS control group, which was a low and negligible result. The B-CQDs (200 μg mL^{-1}) slightly increased the ROS levels in B16F10 cells compared to the other groups. This can be explained by the fact that B-CQD-induced mitochondrial ROS were neutralized by the antioxidants produced in the cells.[51−53] This was also supported by the TUNEL assay, where the B-CQD-treated cells exhibited a negligible

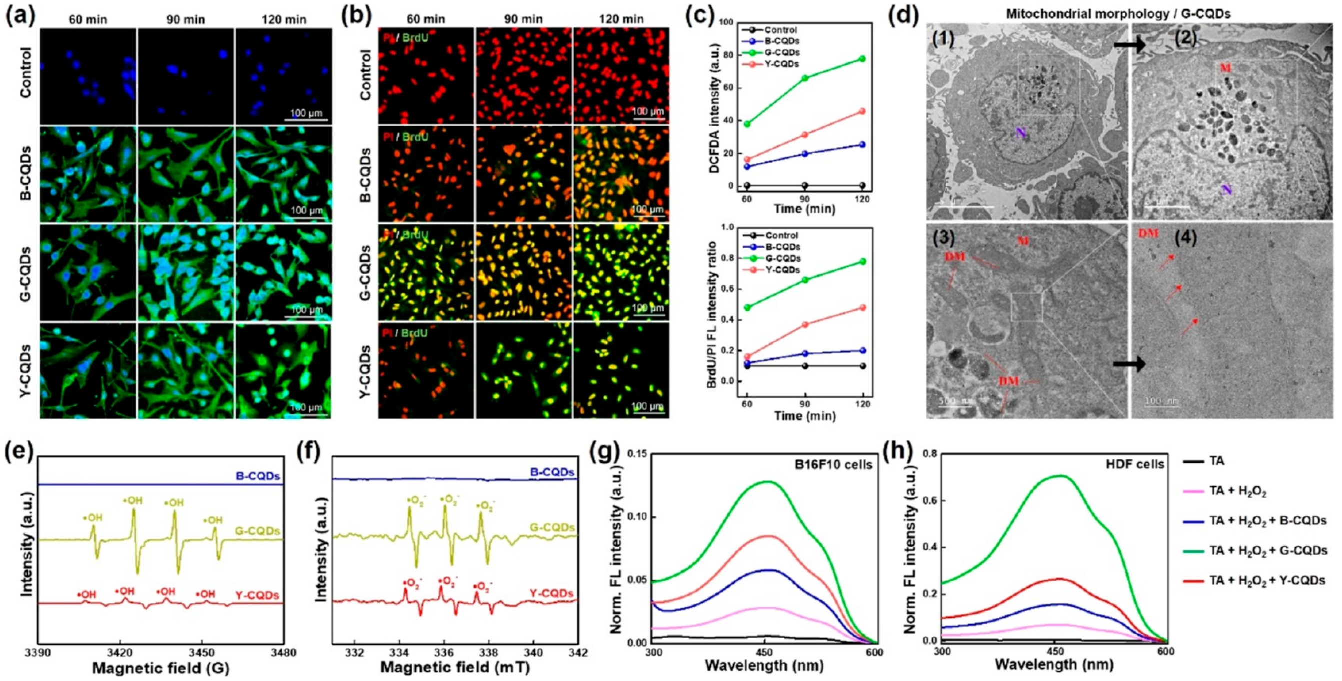

Figure 7. Shape-engineered CQDs enhances oxidative stress and DNA damage in B16F10 melanoma cells. (a) CLSM images of B16F10 cells showing the time-dependent ROS (60, 90, and 120 min) generation (DCFDA staining) and (b) DNA damage (TUNEL assay) in the presence of various CQDs. Scale bar: 100 μm. (c) Quantification data of ROS and TUNEL assays. (d) Bio-TEM image of G-CQDs-treated B16F10 cells with the corresponding magnified views (1−4) showing the presence of malfunctioned and disrupted mitochondria. (e,f) EPR spectra of CQDs showing the hydroxyl ($^\bullet$OH) and single oxygen generation ($^1O_2$) using DMPO or TEMP as a spin trap agent. (g,h) FL spectra of the cell-derived hydroxyl radicals ($^\bullet$OH) and TA after 24 h of cell culture. B16F10 (melanoma/cancer) and HDF (normal/healthy) cells were selected for a side-by-side comparison of ROS generation study.

fluorescence of the BrdU dye, which served as an indicator of DNA damage. Interestingly, the polyphenol containing CQDs (100 μg mL^{-1})-treated B16F10 cells exhibited higher oxidative damage than the B-CQDs after 48 h of incubation. The levels of DCF-DA and BrdU fluorescence were gradually increased in the G-CQD treatment, which is similar to our previous reports[78] without DOX conjugation (Figure S22b). The localization of BrdU (bright green fluorescence) was very specific and intense in G-CQD-treated B16F10 cells, which showed a similar fluorescence pattern to that exhibited by cells treated with an anticancer drug, doxorubicin (Dox).

Next, we performed CLSM at various times to investigate the cause of intracellular ROS and DNA damage. As shown in Figure 7a, CQD-treated cells exhibited very low levels of cytoplasmic ROS after 60 min of incubation. Notably, after 60 min, the intracellular DCF-DA fluorescence significantly increased in a time-dependent manner. The G-CQDs (100 μg mL^{-1}) profoundly affected the ROS amplification in B16F10 cells within a time frame of 60−120 min, while the B- and Y-CQDs maintained a low level of ROS within 90 min of treatment. Our results demonstrate that CQDs induce mitochondrial dysfunction, leading to oxidative stress in mitochondria, which subsequently initiates ROS production in the cytoplasm. The characteristic DCF-DA fluorescence in the cytoplasm was both dose- and time-dependent. The cytoplasmic ROS greatly influenced nuclear DNA damage following CQD treatment. As demonstrated, nuclear DNA damage was also time-dependent (Figure 7b). Before 60 min, BrdU fluorescence was very low in the nucleus in all of the CQD-treated cells. After that, BrdU fluorescence greatly increased with time. The B-CQDs showed a lower FL signal of BrdU within a 60−120 min time frame. The Y-CQDs were found to promote DNA damage after 90 min of incubation, suggesting that incubation time played a crucial role in DNA damage. The quantitative data of ROS and TUNEL assay is given in Figure 7c. Additionally, the BrdU fluorescence was remarkably enhanced following G-CQD treatment as the time increased from 60 to 120 min. This can be explained by the fact that small graphene-like CQDs (containing seven benzene ring structures) tend to interact with the guanine (G) in the DNA, leading to a base mismatch and DNA unwinding. The insertion of G-CQDs leads to the unusual breakage of hydrogen bonds between adenine (A) and thymine (T) bases, resulting in the formation of small DNA fragments inside the nucleus.[50,54−56] To some extent, the graphene CQDs interact with nucleic acid via electrostatic interactions or π−π stacking, which induce DNA damage and upregulation of apoptosis-related genes, such as *Bax* and *Casp*-3.[13] In this study, the CQD-induced DNA damage was also characterized by the early accumulation of damaged DNA, which is due to the cell cycle aberration (late G2/M phase) (Figure S23). These results demonstrate that graphene-like G- and Y-CQDs effectively induce apoptosis in cancer cells via several mechanisms discussed above.[19,25]

Next, to investigate the mitochondrial morphology, CQD-treated B16F10 cells were harvested and analyzed through Bio-TEM. Figure 7d shows that G-CQD (100 μg mL^{-1}) treatment damaged the mitochondrial membrane. The mitochondrial morphology in the presence of various formulations of CQDs is presented in Figure S24. Compared to the untreated B16F10 cells, the Dox-and CQD-treated cells exhibited a decreased mitochondrial perimeter (Figure S25), area (Figure S26a), and length (Figure S26b), indicating that CQDs have significantly halted mitochondrial function. Although the untreated cells

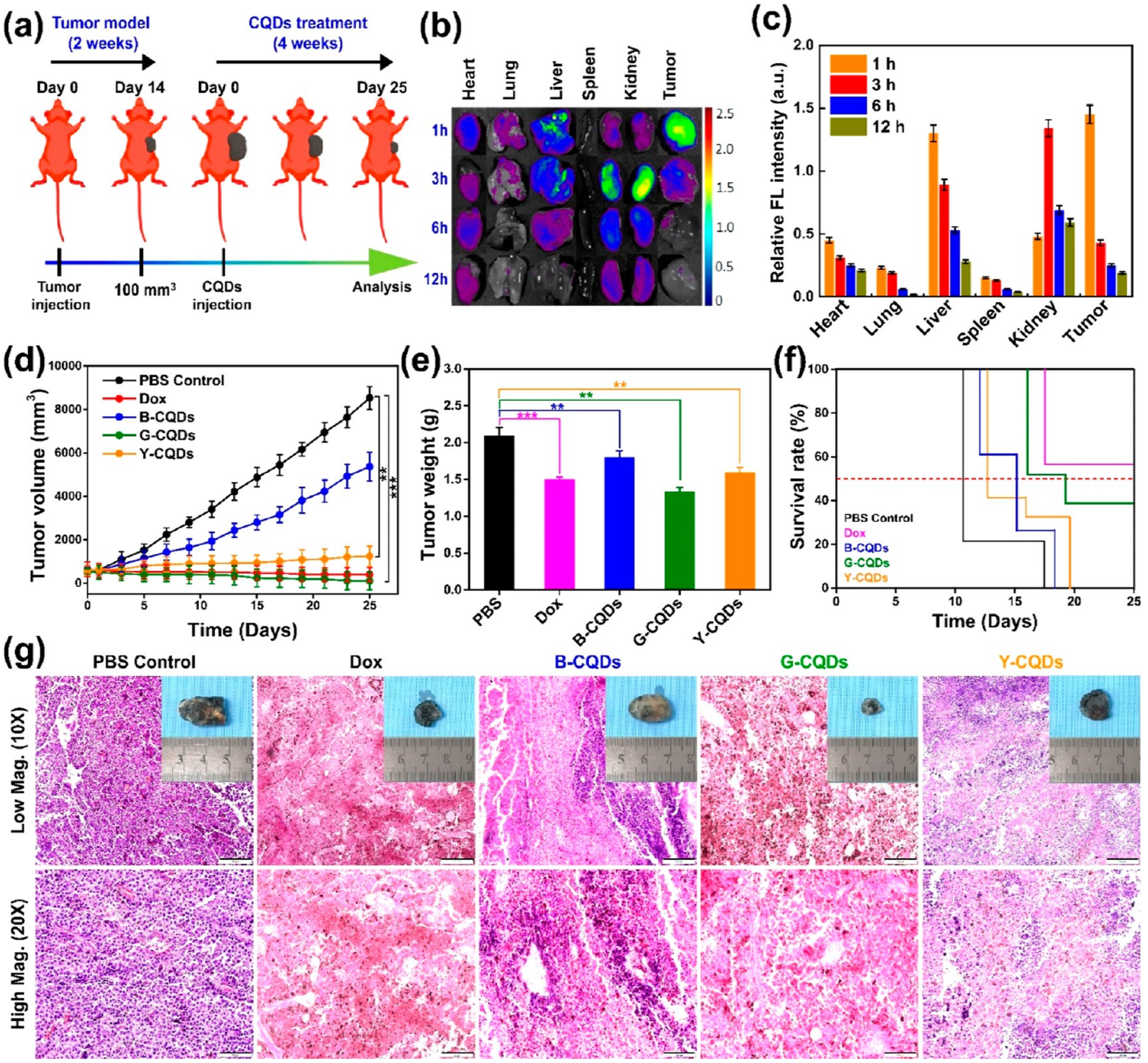

Figure 8. In vivo therapeutic efficiency of shape-engineered CQDs. (a) Schematic presentation showing the formulation of CQDs in BalB/c nude mice subcutaneous tumor models at indicated time points. (b) Ex vivo biodistribution analysis of G-CQDs in various organs isolated from the tumor-bearing mice with (c) corresponding FL intensities, respectively. (d−f) Analysis of the tumor growth curves, tumor volume, and the survival rates in different formulations on day 25. (g) Representative histological images of the tumor tissues after various formulation of CQDs. Tissue sections were stained with H&E. Scale bar: scale bar: 100 and 200 μm. Statistical significance at $^{**}p < 0.01$ and $^{***}p < 0.001$ (Students *t*-test).

showed well-developed cristae in the mitochondrial inner membrane, the cristae completely disappeared in the G-CQD-treated cells (Figure 7d). Moreover, the mitochondrial branching pattern (*F*-factor) was also taken into consideration. With G-CQD exposure, the melanoma cells no longer showed a branched mitochondrial network and after 48 h, the mitochondrial networks were reduced to a short branch, which was indicated with a decrease of *F*-factor value (Figure S27). The treatment with CQDs inhibited mitochondrial respiration by damaging the cristae structure and leakage of the mitochondrial membrane, which ultimately resulted in higher ROS production.[57,58] The CQD-treated cells exhibited a higher fluorescence intensity of MitoTracker Red, which suggests that damaged mitochondria formed an aggregate-like structure and accumulated near the plasma membrane of B16F10 cells (Figure S28). Moreover, we have investigated the GSH activity of B16F10 cells after treatment with various formulations of CQDs, which are shown in Figure S29a. The groups treated with H_2O_2 (200 μM) and Dox (200 μM) were used as the positive control. Initially, there was no decrease in GSH levels after 24 h of CQD treatment. However, cellular GSH was significantly depleted after 48 h of CQD treatment, and the G-CQD treatment resulted in an ∼37% decrease in cellular GSH levels, compared to the untreated cells. Interestingly, the mitochondrial GSH was also reduced by ∼28, ∼78, and ∼70% in B-CQD-, G-CQD-, and Y-CQD-treated cells (Figure S29b). This is because the cancer cells produce an excess amount of GSH compared with the normal cells, and the depletion of GSH levels in cancer cells indicates cell death. In our study, G-CQD treatment selectively depleted the GSH levels in B16F10 cells and amplified the ROS production. Another mechanism of this phenomenon might be the higher affinity of G-CQDs toward the sulfhydryl (SH−) or amine ($-NH_2$) groups of GSH.[59,60] Moreover, we found that the OCR[61] changed drastically after CQD treatment in B16F10 cells. As shown in Figure S29c, the OCR was significantly affected by treatment with G-CQDs after 48 h of incubation, which was comparable to that of the positive control. Considering the fact that ATP is one of the key products of glycolysis,[62] we have also examined the ATP content in B16F10 cell culture media, to determine the metabolism inhibitory potential of the CQDs. Before 48 h, there was no significant decrease in the ATP synthesis rate; however, after 48 h, the ATP production was significantly inhibited in G-CQD- and Y-CQD-treated B16F10 cells (Figure S29d). These findings show that GSH is greatly depleted by the increased oxidative stress brought on by CQDs and decreases oxygen uptake in mitochondria, followed by a sharp decrease in ATP production, which ultimately causes apoptotic cell death.

To further determine the ROS types, the EPR spectra were analyzed in the presence of CQDs using DMPO or TEMP as a spin trapper for hydroxyl ($^\bullet$OH) and singlet oxygen ($^1O_2$) radicals. Figure 7e shows that the polyphenol containing CQDs exhibited characteristic 1:2:2:1 intensity peaks for the $^\bullet$OH radicals. However, the B-CQDs were not found to produce any kind of $^\bullet$OH radical peaks. The $^\bullet$OH radical intensity ratio was found higher in G-CQDs than the Y-CQDs. Our results are consistent with previous reports where the graphitic/carbon nanomaterials showed significant ROS production. Similarly, the detection of $^1O_2$ showed the same result after incubation with CQDs, respectively (Figure 7f). The G-CQD-treated sample showed the characteristic 1:1:1 intensity peak for $^1O_2$ radicals, which was not generated in the case of B-CQDs and a little amount for Y-CQDs. Therefore, we anticipate that the shape-engineered CQDs have a potential effect on ROS generation, leading to oxidative stress-induced death of B16F10 cells.[63] To validate the $^\bullet$OH radical generation, we also investigated the real-time cellular $^\bullet$OH radical generation in cells using a fluorescence probe known as TA. As shown in Figure 7g,h, the CQDs exhibited superior $^\bullet$OH generation capabilities after incubating with B16F10 and HDF cells. Notably, in both the cells the G-CQDs (100 μg mL^{-1}) displayed abundant $^\bullet$OH radicals after 24 h of incubation than the other CQDs. The fluorescence intensity at 450 nm was found to be higher in the case of G-CQDs (λ_{450} = 0.128 and 0.709) following H_2O_2 addition. Because, the G-CQDs exhibited potent cytotoxicity in both cancer and normal cells; therefore, we used an intratumoral route of administration for an in vivo study.

The mitochondria are directly involved in oxidative stress-induced cell death;[5,64] we hypothesized that shape-engineered CQDs might initiate the upregulation of apoptosis-related genes and protein expression. As shown in Figure S30a, G- and Y-CQDs (100 μg mL^{-1})-treated melanoma cells exhibited a higher apoptotic protein marker expression compared to the untreated cells. The G-CQD-treated cells showed enhancement in the protein expression of mitochondrial (Bad, Bax, SMAC, and Cyto-C) (Figure S30b), cytoplasmic (p53, Casp-3, and Casp-8) (Figure S30c), nuclear (XIAP), and membrane-bound (CD40, TNF-α, and TNF-β; Figure S30d) cell death markers, suggesting that G-CQD treatment significantly enhanced both the mitochondrial-dependent[25,65−67] and mitochondrial-independent apoptotic pathways.[2,13] To get insights into the cell death mechanism, we have also performed qRT-PCR analysis, respectively. As shown in Figure S31, the relative mRNA expression of *Casp-3* and *Casp-9* was increased after exposure to CQDs. More interestingly, the 100 μg mL^{-1} dose of G-CQDs significantly elevated the mRNA expression of *Bax* (6-fold), *Casp-3* (10-fold), *Casp-9* (10.5-fold), and *Cyto-C1* (5-fold). Similarly, a decrease in the *Bcl-2* mRNA expression was also observed in various CQD treatment, suggesting that the activation of these gene marker expression is closely connected to the apoptotic cell death in B16F10 cells.[68−71] A hypothetical drawing of CQD-induced DNA damage and ROS amplification is schematically presented in Figure S32.

Motivated by the promising in vitro results, we next studied the in vivo therapeutic efficiency of CQDs in a subcutaneous tumor model. Before that, we have tested the hemocompatibility of the CQDs using mouse red blood cells (RBCs). In contrast to the positive control group, the CQDs demonstrated good blood biocompatibility, as illustrated in Figure S33. The schematic design of the in vivo experiments is depicted in Figure 8a. The antitumor test was carried out using subcutaneously implanted B16F10 tumor-bearing BALB/c nude mice (Figure S34). The quick removal of chemotherapeutic drugs from tumor sites, which reduces the agents' therapeutic efficacy, is one of the major difficulties in nanomaterials-based chemotherapy. An appropriate nanotheranostic drug with improved tumor penetration and retention (EPR) impact could be a successful treatment plan for solid tumor therapy.[72] After 12 h postinjection, we used ex vivo fluorescence imaging to evaluate G-CQDs' biodistribution to verify the EPR effect. The findings are shown in Figure 8b. Our results demonstrated that G-CQD accumulation was higher in the liver and tumor sites compared to other organs within an hour. Also, the accumulation of G-CQDs in the liver gradually decreased after 3 h of treatment. In fact, the level of G-CQD accumulation in the kidneys rose after 1 h and peaked after 3 h. With no detectable accumulation in the spleen, the level of G-CQD accumulation was noticeably lower. After 6 h, the kidney's accumulation of G-CQD steadily diminished. Due to the specific ability of the liver to detoxify foreign compounds and expel them, G-CQDs collected in the liver quickly after administration and were eliminated via the kidneys as urine.[2] The relative fluorescence intensities of G-CQDs from various organs are shown in Figure 8c, respectively.

For the antitumor study, tumor growth was monitored after the second dose and photographed using a digital camera (Figure S35a). During the 25 days of treatment, the relative tumor volume (Figure 8d) and tumor weight (Figure 8e) of the G-CQD and Y-CQD groups decreased, which was comparable to the observations in the positive control group. However, B-CQDs showed no obvious influence on the decrease in tumor growth, which suggests that B-CQDs have negligible effects on tumor inhibition. The improved efficiency of G-CQDs and Y-CQDs is most likely attributable to the tumor cells' efficient death as a result of the blood vessel's quick immobilization.[19,65,73−75] Besides, no noticeable change in body weight was observed after CQD treatment in various groups (Figure S35b). These results suggest that the formulated dose of CQDs has negligible systemic toxicity in the body. In addition, the mice treated with G-CQDs showed

https://doi.org/10.1021/acsami.3c07547
ACS Appl. Mater. Interfaces 2023, 15, 52083−52099

the highest survival rate compared to that in Dox-treated groups (Figure 8f). Furthermore, the B-CQD-treated groups showed the lowest survival rate compared to the polyphenol containing CQD groups. The biocompatibility of the polymer-like B-CQDs is likely the main cause of the mice's short lifespan.[76,77] Thus, the 200 μg mL^{-1} formulation of B-CQDs showed less tumor-targeting and damaging effects on the tumor site, instead of promoting the tumor growth and, therefore, the eventual death of mice.

Upon completion of the treatment regimen on day 25, mice from each experimental group were subjected to euthanasia, and afterward, tumor tissues were collected for further analysis. The deceased mice from each experimental group were excluded from the in vivo tests. Blood samples were collected from mice to study the biochemical parameters. As shown in Figure S35c,d, there were no detectable pathological abnormalities in the complete blood count (CBC) and complete platelet count (CPC). There was no significant change in the blood profile among the various groups. However, a slight decrease in the platelet count (PLT) was observed in the Dox-, B-CQD-, and G-CQD-treated groups. The Y-CQD-treated mice showed no observable PLT count abnormalities. After 25 days of G-CQD (100 g mL^{-1}) therapy, the liver function index (LFT), which includes indicators such as alkaline phosphatase (ALP), aspartate aminotransferase (AST), alanine aminotransferase (ALT), and renal urea—nitrogen index (BUN), was assessed. The findings are shown in Table S3. Compared to the control groups, our findings demonstrated that all blood indicators relating to the liver and kidneys were within the normal reference ranges. A slight increase in the ALT (101.24 ± 3.6 U/L) and AST (190.3 ± 4.9 U/L) levels was observed in G-CQD-treated group, suggesting that G-CQDs exhibited slight toxicity in the kidney, liver, heart, and blood after prolonged treatments, due to excessive protein intake or organ-specific accumulation of CQDs. Next, we performed the H&E staining of tumor sites to investigate the therapeutic efficiency of the CQDs. Histopathological images of the corresponding dissected tumors are shown in Figure 8g. The H&E staining images of the tumor site at 7 and 14 days of treatment are shown in Figure S36. In the early days of treatment, there was no noticeable change in the morphology of the tissue. However, prolonged treatment with various CQDs significantly altered the tumor cell viability, as shown in Figure 8g. The Dox-treated (5 mg kg^{-1}) and G-CQD-treated (100 μg mL^{-1}) groups exhibited remarkable destruction of tumor cells, particularly the nucleus. An abnormal tissue arrangement, characterized by cell necrosis, lysis, and pyknosis, was observed in the Dox-, G-CQD-, and Y-CQD-treated groups, indicating stress amplification and apoptotic cell death in the B16F10 cells. Apoptotic cell death was negligible in B-CQDs, where a regular tumor growth was observed. Taken together, our results suggest that graphene-like G-CQDs have a significant impact on tumor cell fate and are safe for in vivo antitumor applications.

4. CONCLUSIONS

In conclusion, we developed shape-engineered CQDs (B-CQDs, G-CQDs, and Y-CQDs) and assessed their effectiveness in solid cancer treatment. B-CQDs (spherical) and G-CQDs' (trilateral and quadrilateral; planner) geometries allow high-quality TP imaging of B16F10 melanoma cancer cells and amplify higher oxidative stress through hydroxyl and singlet oxygen radicals, leading to cellular and mitochondrial dysfunction and dose-dependent genotoxicity. Moreover, a single dose of G-CQDs (100 μg mL^{-1}) is sufficient to deplete the GSH and ATP levels in B16F10 cells, allowing extreme sensitivity toward cancer cells. Furthermore, the as-prepared CQDs are effectively cleared from the body, indicating a very low biotoxicity during intratumoral administration. This research investigates the possible use of different shape-engineered CQDs and presents a diverse carbon-based nanomaterial option for cancer nanotheranostics. Furthermore, this proposal proposes that these CQDs might serve as an efficient platform for drug administration. A comparative summary describing the potential use of various CQDs as nanotheranostic agents including the present study is highlighted in Table S4.

ASSOCIATED CONTENT

Data Availability Statement

The primary data necessary to substantiate these results may be obtained from the associated authors upon request.

Supporting Information

The Supporting Information is available free of charge at https://pubs.acs.org/doi/10.1021/acsami.3c07547.

> Schematic illustration of CQD formation mechanism; digital photographs of the CQDs; NMR spectra of the CQDs; zeta potential (ζ) of the CQDs; HR-TEM images of the G- and Y-CQDs; XRD spectra of the CQDs; O 1s XPS spectra of the CQDs; excitation-dependent PL emission spectra of the CQDs; structure of the G-CQDs; structure of the Y-CQDs; band gap energies of the CQDs from the DFT study; dispersion stability of the CQDs; relative fluorescence intensities of the CQDs after treatment with B16F10 cells; multicolor bioimaging property of the CQDs in RBL2H3 and B16F10 cells; photostability measurement of the CQDs; intensity-based pseudocolor images of the B16F10 mitochondria at indicated time points; in vitro cytotoxicity of B16F10 cells in the presence of CQDs; colony formation assay of the B16F10 cells after CQD treatment; in vitro cell migration assays; in vitro cell invasion assays; DCF-DA and TUNEL staining of B16F10 cells after 24 and 48 h of CQD treatment; cell cycle distribution analysis of B16F10; Bio-TEM analysis of the CQD-treated B16F10 cells showing the mitochondrial damage; calculation of mitochondrial perimeter; calculation of average mitochondrial area and length of the B16F10 cells after CQD treatment; calculation of mitochondrial form factor (F); Mito-Tracker deep red staining of B16F10 cells after CQD treatment; effect of CQDs on metabolism of B16F10 cells; quantification of apoptosis-related protein expression; qRT-PCR analysis of the apoptosis-related gene marker expression; mechanism of G-CQD-induced in vitro anticancer effect; hemolysis test of the CQDs; digital photographs of the in vivo tumor model generation; in vivo antitumor properties of the CQDs; H&E staining of the tumor tissues after 7 and 14 days of CQD treatment; gene primer list used for qRT-PCR analysis in this study; TPE cross-section, quantum yield, and FL lifetime of the CQDs at an excitation wavelength of 800 nm; blood biochemistry of the G-CQD-treated mice; and comparative study of various CQDs for tumor therapy (PDF)

AUTHOR INFORMATION

Corresponding Authors

Jongsung Kim − *Department of Chemical and Biological Engineering, Gachon University, Seongnam, Gyeonggi-do 1342, Republic of Korea;* orcid.org/0000-0001-8885-0533; Email: jongkim@gachon.ac.kr

Ki-Taek Lim − *Department of Biosystems Engineering, College of Agriculture and Life Sciences, Kangwon National University, Chuncheon, Gangwon-do 24341, Republic of Korea; Interdisciplinary Program in Smart Agriculture, Kangwon National University, Chuncheon, Gangwon-do 24341, Republic of Korea;* orcid.org/0000-0003-2091-788X; Email: ktlim@kangwon.ac.kr

Authors

Sayan Deb Dutta − *Department of Biosystems Engineering, College of Agriculture and Life Sciences and Institute of Forest Science, Kangwon National University, Chuncheon, Gangwon-do 24341, Republic of Korea*

Md Moniruzzaman − *Department of Chemical and Biological Engineering, Gachon University, Seongnam, Gyeonggi-do 1342, Republic of Korea*

Jin Hexiu − *Department of Plastic and Traumatic Surgery, Capital Medical University, Beijing 100069, China*

Sourav Sarkar − *Department of Chemistry, Pohang University of Science and Technology, Pohang, Gyungbuk 37673, Republic of Korea*

Keya Ganguly − *Department of Biosystems Engineering, College of Agriculture and Life Sciences, Kangwon National University, Chuncheon, Gangwon-do 24341, Republic of Korea*

Dinesh K. Patel − *School of Chemical Engineering, Yeungnam University, 280-Daehak-ro, Gyeongsan 38541, Republic of Korea*

Jagannath Mondal − *Department of Green Bioengineering, Korea National University of Transportation, Chungju 27470, Republic of Korea*

Yong-Kyu Lee − *Department of Green Bioengineering, Korea National University of Transportation, Chungju 27470, Republic of Korea;* orcid.org/0000-0001-8336-3592

Rumi Acharya − *Interdisciplinary Program in Smart Agriculture, Kangwon National University, Chuncheon, Gangwon-do 24341, Republic of Korea*

Complete contact information is available at: https://pubs.acs.org/10.1021/acsami.3c07547

Author Contributions

$^{\nabla}$S.D.D., M.M. and J.H. are contributed equally to this manuscript.

Notes

The authors declare no competing financial interest.

ACKNOWLEDGMENTS

The authors express their appreciation on the underlying support in Bio-TEM analysis from Mrs. Myung-Seon Jeong, Korea Basic Science Institute (KBSI), Chuncheon Center, Republic of Korea. The authors would like to thank the "Central Instrumentation" of Kangwon National University for the help of Confocal Microscopy and FACS analysis. This work was supported by the "Basic Research Program" through the "National Research Foundation of Korea (NRF)" funded by the "Ministry of Education" (grant nos. 2018R1A6A1A03025582, 2019R1D1A3A03103828, and 2022R1I1A3063302). This research was also supported by the Basic Science Research Program through the National Research Foundation of Korea (NRF) funded by the Ministry of Education (grant nos. 2021R1A6A1A03038996 and 2022R1G1A1010780). This work was also supported by the grants received from the "National Natural Science Foundation of China" (grant no. 81700926) and Beijing Hospitals Authority Youth Program (grant no. QML2019503).

REFERENCES

(1) Shi, Y. A structural view of mitochondria-mediated apoptosis. *Nat. Struct. Biol.* **2001**, *8* (5), 394−401.

(2) Gong, N.; Ma, X.; Ye, X.; Zhou, Q.; Chen, X.; Tan, X.; Yao, S.; Huo, S.; Zhang, T.; Chen, S.; et al. Carbon-dot-supported atomically dispersed gold as a mitochondrial oxidative stress amplifier for cancer treatment. *Nat. Nanotechnol.* **2019**, *14* (4), 379−387.

(3) Geng, X.; Sun, Y.; Li, Z.; Yang, R.; Zhao, Y.; Guo, Y.; Xu, J.; Li, F.; Wang, Y.; Lu, S.; et al. Retrosynthesis of tunable fluorescent carbon dots for precise long-term mitochondrial tracking. *Small* **2019**, *15* (48), 1901517.

(4) Zhu, Z.-J.; Yeh, Y.-C.; Tang, R.; Yan, B.; Tamayo, J.; Vachet, R. W.; Rotello, V. M. Stability of quantum dots in live cells. *Nat. Chem.* **2011**, *3* (12), 963−968.

(5) Sabharwal, S. S.; Schumacker, P. T. Mitochondrial ROS in cancer: initiators, amplifiers or an Achilles' heel? *Nat. Rev. Cancer* **2014**, *14* (11), 709−721.

(6) Wallace, D. C. Mitochondria and cancer. *Nat. Rev. Cancer* **2012**, *12* (10), 685−698.

(7) Xu, J.; Zeng, F.; Wu, H.; Hu, C.; Yu, C.; Wu, S. Preparation of a mitochondria-targeted and NO-releasing nanoplatform and its enhanced pro-apoptotic effect on cancer cells. *Small* **2014**, *10* (18), 3750−3760.

(8) Wolf, D. A. Is reliance on mitochondrial respiration a "chink in the armor" of therapy-resistant cancer? *Cancer Cell* **2014**, *26* (6), 788−795.

(9) Ciccarese, F.; Ciminale, V. Escaping death: mitochondrial redox homeostasis in cancer cells. *Front. Oncol.* **2017**, *7*, 117.

(10) Wang, H.; Feng, Z.; Wang, Y.; Zhou, R.; Yang, Z.; Xu, B. Integrating enzymatic self-assembly and mitochondria targeting for selectively killing cancer cells without acquired drug resistance. *J. Am. Chem. Soc.* **2016**, *138* (49), 16046−16055.

(11) Wang, D.; Wu, H.; Phua, S. Z. F.; Yang, G.; Qi Lim, W.; Gu, L.; Qian, C.; Wang, H.; Guo, Z.; Chen, H.; et al. Self-assembled single-atom nanozyme for enhanced photodynamic therapy treatment of tumor. *Nat. Commun.* **2020**, *11* (1), 357.

(12) Wu, C.; Wang, C.; Han, T.; Zhou, X.; Guo, S.; Zhang, J. Insight into the cellular internalization and cytotoxicity of graphene quantum dots. *Adv. Healthcare Mater.* **2013**, *2* (12), 1613−1619.

(13) Qi, L.; Pan, T.; Ou, L.; Ye, Z.; Yu, C.; Bao, B.; Wu, Z.; Cao, D.; Dai, L. Biocompatible nucleus-targeted graphene quantum dots for selective killing of cancer cells via DNA damage. *Commun. Biol.* **2021**, *4* (1), 214.

(14) Gao, X.; Cui, Y.; Levenson, R. M.; Chung, L. W.; Nie, S. In vivo cancer targeting and imaging with semiconductor quantum dots. *Nat. Biotechnol.* **2004**, *22* (8), 969−976.

(15) He, H.; Fei, Z.; Guo, T.; Hou, Y.; Li, D.; Wang, K.; Ren, F.; Fan, K.; Zhou, D.; Xie, C.; et al. Bioadhesive injectable hydrogel with phenolic carbon quantum dot supported Pd single atom nanozymes as a localized immunomodulation niche for cancer catalytic immunotherapy. *Biomaterials* **2022**, *280*, 121272.

(16) Gui, X.; Chen, Y.; Zhang, Z.; Lei, L.; Zhu, F.; Yang, W.; Guo, Y.; Chu, M. Fluorescent hollow mesoporous carbon spheres for drug loading and tumor treatment through 980-nm laser and microwave co-irradiation. *Biomaterials* **2020**, *248*, 120009.

(17) Chu, M.; Pan, X.; Zhang, D.; Wu, Q.; Peng, J.; Hai, W. The therapeutic efficacy of CdTe and CdSe quantum dots for photothermal cancer therapy. *Biomaterials* **2012**, *33* (29), 7071−7083.

(18) Huang, Y.; Fan, C.-Q.; Dong, H.; Wang, S.-M.; Yang, X.-C.; Yang, S.-M. Current applications and future prospects of nanomaterials in tumor therapy. *Int. J. Nanomed.* **2017**, *12*, 1815−1825.

(19) Ge, J.; Lan, M.; Zhou, B.; Liu, W.; Guo, L.; Wang, H.; Jia, Q.; Niu, G.; Huang, X.; Zhou, H.; et al. A graphene quantum dot photodynamic therapy agent with high singlet oxygen generation. *Nat. Commun.* **2014**, *5* (1), 4596.

(20) Đorđević, L.; Arcudi, F.; Cacioppo, M.; Prato, M. A multifunctional chemical toolbox to engineer carbon dots for biomedical and energy applications. *Nat. Nanotechnol.* **2022**, *17* (2), 112−130.

(21) Moniruzzaman, M.; Anantha Lakshmi, B.; Kim, S.; Kim, J. Preparation of shape-specific (trilateral and quadrilateral) carbon quantum dots towards multiple color emission. *Nanoscale* **2020**, *12* (22), 11947−11959.

(22) Wu, F.; Su, H.; Cai, Y.; Wong, W.-K.; Jiang, W.; Zhu, X. Porphyrin-implanted carbon nanodots for photoacoustic imaging and in vivo breast cancer ablation. *ACS Appl. Bio Mater.* **2018**, *1* (1), 110−117.

(23) Wu, F.; Chen, J.; Yue, L.; Li, H.; Wang, H.; Zhu, X. A Simple Strategy to Fabricate Phthalocyanine-Encapsulated Nanodots for Magnetic Resonance Imaging and Antitumor Phototherapy. *ACS Appl. Bio Mater.* **2020**, *3* (6), 3681−3689.

(24) Wang, D.; Zhu, L.; Chen, J.-F.; Dai, L. Can graphene quantum dots cause DNA damage in cells? *Nanoscale* **2015**, *7* (21), 9894−9901.

(25) Zhang, D.; Wen, L.; Huang, R.; Wang, H.; Hu, X.; Xing, D. Mitochondrial specific photodynamic therapy by rare-earth nanoparticles mediated near-infrared graphene quantum dots. *Biomaterials* **2018**, *153*, 14−26.

(26) Zhang, Y.; He, Y.; Cui, P.; Feng, X.; Chen, L.; Yang, Y.; Liu, X. Water-soluble, nitrogen-doped fluorescent carbon dots for highly sensitive and selective detection of Hg 2+ in aqueous solution. *RSC Adv.* **2015**, *5* (50), 40393−40401.

(27) Yuan, F.; Yuan, T.; Sui, L.; Wang, Z.; Xi, Z.; Li, Y.; Li, X.; Fan, L.; Tan, Z. a.; Chen, A.; et al. Engineering triangular carbon quantum dots with unprecedented narrow bandwidth emission for multicolored LEDs. *Nat. Commun.* **2018**, *9* (1), 2249.

(28) Ganguly, K.; Jin, H.; Dutta, S. D.; Patel, D. K.; Patil, T. V.; Lim, K.-T. Magnetic field-assisted aligned patterning in an alginate-silk fibroin/nanocellulose composite for guided wound healing. *Carbohydr. Polym.* **2022**, *287*, 119321.

(29) Dutta, S. D.; Patel, D. K.; Seo, Y.-R.; Park, C.-W.; Lee, S.-H.; Kim, J.-W.; Kim, J.; Seonwoo, H.; Lim, K.-T. In vitro biocompatibility of electrospun poly (ε-caprolactone)/cellulose nanocrystals-nanofibers for tissue engineering. *J. Nanomater.* **2019**, *2019*, 2061545.

(30) Holubova, M.; Konefał, R.; Moravkova, Z.; Zhigunov, A.; Svoboda, J.; Pop-Georgievski, O.; Hromadkova, J.; Groborz, O.; Stepanek, P.; Hruby, M. Carbon nanospecies affecting amyloid formation. *RSC Adv.* **2017**, *7* (85), 53887−53898.

(31) Wang, L.; Li, W.; Yin, L.; Liu, Y.; Guo, H.; Lai, J.; Han, Y.; Li, G.; Li, M.; Zhang, J.; et al. Full-color fluorescent carbon quantum dots. *Sci. Adv.* **2020**, *6* (40), No. eabb6772.

(32) Niu, Q.; Gao, K.; Lin, Z.; Wu, W. Amine-capped carbon dots as a nanosensor for sensitive and selective detection of picric acid in aqueous solution via electrostatic interaction. *Anal. Methods* **2013**, *5* (21), 6228−6233.

(33) Wang, L.; Wang, Y.; Xu, T.; Liao, H.; Yao, C.; Liu, Y.; Li, Z.; Chen, Z.; Pan, D.; Sun, L.; et al. Gram-scale synthesis of single-crystalline graphene quantum dots with superior optical properties. *Nat. Commun.* **2014**, *5* (1), 5357.

(34) Taspika, M.; Permatasari, F. A.; Nuryadin, B. W.; Mayangsari, T. R.; Aimon, A. H.; Iskandar, F. Simultaneous ultraviolet and first near-infrared window absorption of luminescent carbon dots/PVA composite film. *RSC Adv.* **2019**, *9* (13), 7375−7381.

(35) Estes, C. S.; Gerard, A. Y.; Godward, J. D.; Hayes, S. B.; Liles, S. H.; Shelton, J. L.; Stewart, T. S.; Webster, R. I.; Webster, H. F. Preparation of highly functionalized carbon nanoparticles using a one-step acid dehydration of glycerol. *Carbon* **2019**, *142*, 547−557.

(36) Fuente, E.; Menéndez, J. A.; Díez, M. A.; Suárez, D.; Montes-Morán, M. A. Infrared spectroscopy of carbon materials: a quantum chemical study of model compounds. *J. Phys. Chem. B* **2003**, *107* (26), 6350−6359.

(37) Suganuma, S.; Nakajima, K.; Kitano, M.; Yamaguchi, D.; Kato, H.; Hayashi, S.; Hara, M. Hydrolysis of cellulose by amorphous carbon bearing SO3H, COOH, and OH groups. *J. Am. Chem. Soc.* **2008**, *130* (38), 12787−12793.

(38) Li, B.; Wu, C.; Wang, M.; Charan, K.; Xu, C. An adaptive excitation source for high-speed multiphoton microscopy. *Nat. Methods* **2020**, *17* (2), 163−166.

(39) Zhu, S.; Wang, L.; Zhou, N.; Zhao, X.; Song, Y.; Maharjan, S.; Zhang, J.; Lu, L.; Wang, H.; Yang, B. The crosslink enhanced emission (CEE) in non-conjugated polymer dots: from the photoluminescence mechanism to the cellular uptake mechanism and internalization. *Chem. Commun.* **2014**, *50* (89), 13845−13848.

(40) Liu, H.; Lv, X.; Qian, J.; Li, H.; Qian, Y.; Wang, X.; Meng, X.; Lin, W.; Wang, H. Graphitic Carbon Nitride Quantum Dots Embedded in Carbon Nanosheets for Near-Infrared Imaging-Guided Combined Photo-Chemotherapy. *ACS Nano* **2020**, *14* (10), 13304−13315.

(41) Han, G.; Zhao, J.; Zhang, R.; Tian, X.; Liu, Z.; Wang, A.; Liu, R.; Liu, B.; Han, M. Y.; Gao, X.; et al. Membrane-penetrating carbon quantum dots for imaging nucleic acid structures in live organisms. *Angew. Chem., Int. Ed.* **2019**, *58* (21), 7087−7091.

(42) Jung, Y. K.; Shin, E.; Kim, B.-S. Cell nucleus-targeting zwitterionic carbon dots. *Sci. Rep.* **2015**, *5* (1), 18807.

(43) Unnikrishnan, B.; Wu, R.-S.; Wei, S.-C.; Huang, C.-C.; Chang, H.-T. Fluorescent carbon dots for selective labeling of subcellular organelles. *ACS Omega* **2020**, *5* (20), 11248−11261.

(44) Hua, X.-W.; Bao, Y.-W.; Chen, Z.; Wu, F.-G. Carbon quantum dots with intrinsic mitochondrial targeting ability for mitochondria-based theranostics. *Nanoscale* **2017**, *9* (30), 10948−10960.

(45) Jin, Y.-R.; Liu, Y.; Jiang, F.-L. Positive Sorption Behaviors in the Ligand Exchanges for Water-Soluble Quantum Dots and a Strategy for Specific Targeting. *ACS Appl. Mater. Interfaces* **2021**, *13* (43), 51746−51758.

(46) Gao, G.; Jiang, Y.-W.; Yang, J.; Wu, F.-G. Mitochondria-targetable carbon quantum dots for differentiating cancerous cells from normal cells. *Nanoscale* **2017**, *9* (46), 18368−18378.

(47) Shen, Y.; Zhang, X.; Liang, L.; Yue, J.; Huang, D.; Xu, W.; Shi, W.; Liang, C.; Xu, S. Mitochondria-targeting supra-carbon dots: Enhanced photothermal therapy selective to cancer cells and their hyperthermia molecular actions. *Carbon* **2020**, *156*, 558−567.

(48) Pieper, H.; Chercheja, S.; Eigler, S.; Halbig, C. E.; Filipovic, M. R.; Mokhir, A. Endoperoxides revealed as origin of the toxicity of graphene oxide. *Angew. Chem., Int. Ed.* **2016**, *55* (1), 405−407.

(49) Rosli, N. F.; Fojtů, M.; Fisher, A. C.; Pumera, M. Graphene oxide nanoplatelets potentiate anticancer effect of cisplatin in human lung cancer cells. *Langmuir* **2019**, *35* (8), 3176−3182.

(50) Chong, Y.; Ma, Y.; Shen, H.; Tu, X.; Zhou, X.; Xu, J.; Dai, J.; Fan, S.; Zhang, Z. The in vitro and in vivo toxicity of graphene quantum dots. *Biomaterials* **2014**, *35* (19), 5041−5048.

(51) Kasouni, A. I.; Chatzimitakos, T. G.; Troganis, A. N.; Stalikas, C. D. Citric acid-based carbon dots: From revealing new insights into their biological properties to demonstrating their enhanced wound healing potential by in vitro and in vivo experiments. *Mater. Today Commun.* **2021**, *26*, 102019.

(52) Das, P.; Ganguly, S.; Margel, S.; Gedanken, A. Immobilization of Heteroatom-Doped Carbon Dots onto Nonpolar Plastics for Antifogging, Antioxidant, and Food Monitoring Applications. *Langmuir* **2021**, *37* (11), 3508−3520.

(53) Dehvari, K.; Chiu, S.-H.; Lin, J.-S.; Girma, W. M.; Ling, Y.-C.; Chang, J.-Y. Heteroatom doped carbon dots with nanoenzyme like properties as theranostic platforms for free radical scavenging, imaging, and chemotherapy. *Acta Biomater.* **2020**, *114*, 343−357.

(54) Kong, Z.; Hu, W.; Jiao, F.; Zhang, P.; Shen, J.; Cui, B.; Wang, H.; Liang, L. Theoretical Evaluation of DNA Genotoxicity of Graphene Quantum Dots: A Combination of Density Functional

Theory and Molecular Dynamics Simulations. *J. Phys. Chem. B* **2020**, *124* (42), 9335−9342.

(55) Liang, L.; Peng, X.; Sun, F.; Kong, Z.; Shen, J.-W. A review on the cytotoxicity of graphene quantum dots: from experiment to simulation. *Nanoscale Adv.* **2021**, *3* (4), 904−917.

(56) Wu, T.; Liang, X.; Liu, X.; Li, Y.; Wang, Y.; Kong, L.; Tang, M. Induction of ferroptosis in response to graphene quantum dots through mitochondrial oxidative stress in microglia. *Part. Fibre Toxicol.* **2020**, *17* (1), 30.

(57) Labuschagne, C. F.; Cheung, E. C.; Blagih, J.; Domart, M.-C.; Vousden, K. H. Cell clustering promotes a metabolic switch that supports metastatic colonization. *Cell Metab.* **2019**, *30* (4), 720−734.e5.

(58) Ma, X.; Hartmann, R.; Jimenez de Aberasturi, D.; Yang, F.; Soenen, S. J.; Manshian, B. B.; Franz, J.; Valdeperez, D.; Pelaz, B.; Feliu, N.; et al. Colloidal gold nanoparticles induce changes in cellular and subcellular morphology. *ACS Nano* **2017**, *11* (8), 7807−7820.

(59) Deng, S.; Fu, A.; Junaid, M.; Wang, Y.; Yin, Q.; Fu, C.; Liu, L.; Su, D.-S.; Bian, W.-P.; Pei, D.-S. Nitrogen-doped graphene quantum dots (N-GQDs) perturb redox-sensitive system via the selective inhibition of antioxidant enzyme activities in zebrafish. *Biomaterials* **2019**, *206*, 61−72.

(60) Li, R.; Guiney, L. M.; Chang, C. H.; Mansukhani, N. D.; Ji, Z.; Wang, X.; Liao, Y.-P.; Jiang, W.; Sun, B.; Hersam, M. C.; et al. Surface oxidation of graphene oxide determines membrane damage, lipid peroxidation, and cytotoxicity in macrophages in a pulmonary toxicity model. *ACS Nano* **2018**, *12* (2), 1390−1402.

(61) Alavian, K. N.; Li, H.; Collis, L.; Bonanni, L.; Zeng, L.; Sacchetti, S.; Lazrove, E.; Nabili, P.; Flaherty, B.; Graham, M.; et al. Bcl-x L regulates metabolic efficiency of neurons through interaction with the mitochondrial F 1 FO ATP synthase. *Nat. Cell Biol.* **2011**, *13* (10), 1224−1233.

(62) Luengo, A.; Li, Z.; Gui, D. Y.; Sullivan, L. B.; Zagorulya, M.; Do, B. T.; Ferreira, R.; Naamati, A.; Ali, A.; Lewis, C. A.; et al. Increased demand for NAD+ relative to ATP drives aerobic glycolysis. *Mol. Cell* **2021**, *81* (4), 691−707.e6.

(63) Du, F.; Liu, L.; Li, L.; Huang, J.; Wang, L.; Tang, Y.; Ke, B.; Song, L.; Cheng, C.; Ma, L.; et al. Conjugated Coordination Porphyrin-based Nanozymes for Photo-/Sono-Augmented Biocatalytic and Homologous Tumor Treatments. *ACS Appl. Mater. Interfaces* **2021**, *13* (35), 41485−41497.

(64) Kroemer, G.; Reed, J. C. Mitochondrial control of cell death. *Nat. Med.* **2000**, *6* (5), 513−519.

(65) Ruan, J.; Wang, Y.; Li, F.; Jia, R.; Zhou, G.; Shao, C.; Zhu, L.; Cui, M.; Yang, D.-P.; Ge, S. Graphene quantum dots for radiotherapy. *ACS Appl. Mater. Interfaces* **2018**, *10* (17), 14342−14355.

(66) Markovic, Z. M.; Ristic, B. Z.; Arsikin, K. M.; Klisic, D. G.; Harhaji-Trajkovic, L. M.; Todorovic-Markovic, B. M.; Kepic, D. P.; Kravic-Stevovic, T. K.; Jovanovic, S. P.; Milenkovic, M. M.; et al. Graphene quantum dots as autophagy-inducing photodynamic agents. *Biomaterials* **2012**, *33* (29), 7084−7092.

(67) Ge, J.; Jia, Q.; Liu, W.; Guo, L.; Liu, Q.; Lan, M.; Zhang, H.; Meng, X.; Wang, P. Red-emissive carbon dots for fluorescent, photoacoustic, and thermal theranostics in living mice. *Adv. Mater.* **2015**, *27* (28), 4169−4177.

(68) Shang, Y.; Wang, Q.; Wu, B.; Zhao, Q.; Li, J.; Huang, X.; Chen, W.; Gui, R. Platelet-membrane-camouflaged black phosphorus quantum dots enhance anticancer effect mediated by apoptosis and autophagy. *ACS Appl. Mater. Interfaces* **2019**, *11* (31), 28254−28266.

(69) Ganesh, S.; Venkatakrishnan, K.; Tan, B. Quantum scale organic semiconductors for SERS detection of DNA methylation and gene expression. *Nat. Commun.* **2020**, *11* (1), 1135.

(70) Ambrosone, A.; Mattera, L.; Marchesano, V.; Quarta, A.; Susha, A. S.; Tino, A.; Rogach, A. L.; Tortiglione, C. Mechanisms underlying toxicity induced by CdTe quantum dots determined in an invertebrate model organism. *Biomaterials* **2012**, *33* (7), 1991−2000.

(71) Noh, J.; Kwon, B.; Han, E.; Park, M.; Yang, W.; Cho, W.; Yoo, W.; Khang, G.; Lee, D. Amplification of oxidative stress by a dual stimuli-responsive hybrid drug enhances cancer cell death. *Nat. Commun.* **2015**, *6* (1), 6907.

(72) Shao, J.; Xie, H.; Huang, H.; Li, Z.; Sun, Z.; Xu, Y.; Xiao, Q.; Yu, X.-F.; Zhao, Y.; Zhang, H.; et al. Biodegradable black phosphorus-based nanospheres for in vivo photothermal cancer therapy. *Nat. Commun.* **2016**, *7* (1), 12967.

(73) Zheng, M.; Liu, S.; Li, J.; Qu, D.; Zhao, H.; Guan, X.; Hu, X.; Xie, Z.; Jing, X.; Sun, Z. Integrating oxaliplatin with highly luminescent carbon dots: an unprecedented theranostic agent for personalized medicine. *Adv. Mater.* **2014**, *26* (21), 3554−3560.

(74) Feng, T.; Ai, X.; An, G.; Yang, P.; Zhao, Y. Charge-convertible carbon dots for imaging-guided drug delivery with enhanced in vivo cancer therapeutic efficiency. *ACS Nano* **2016**, *10* (4), 4410−4420.

(75) Hou, L.; Chen, D.; Wang, R.; Wang, R.; Zhang, H.; Zhang, Z.; Nie, Z.; Lu, S. Transformable Honeycomb-Like Nanoassemblies of Carbon Dots for Regulated Multisite Delivery and Enhanced Antitumor Chemoimmunotherapy. *Angew. Chem., Int. Ed.* **2021**, *60* (12), 6581−6592.

(76) Liu, Q.; Guo, B.; Rao, Z.; Zhang, B.; Gong, J. R. Strong two-photon-induced fluorescence from photostable, biocompatible nitrogen-doped graphene quantum dots for cellular and deep-tissue imaging. *Nano Lett.* **2013**, *13* (6), 2436−2441.

(77) Jiang, K.; Sun, S.; Zhang, L.; Wang, Y.; Cai, C.; Lin, H. Bright-yellow-emissive N-doped carbon dots: preparation, cellular imaging, and bifunctional sensing. *ACS Appl. Mater. Interfaces* **2015**, *7* (41), 23231−23238.

(78) Dutta, S. D.; Hexiu, J.; Kim, J. S.; Sarkar, S.; Mondal, J.; An, J. M.; Lee, Y.-K.; Moniruzzaman, M.; Lim, K.-T. Two-photon excitable membrane targeting polyphenolic carbon dots for long-term imaging and pH-responsive chemotherapeutic drug delivery for synergistic tumor therapy. *Biomater. Sci.* **2022**, *10*, 1680−1696.